Peral Mireia (Orcid ID: 0000-0001-8026-2753)

Ruh Jonas (Orcid ID: 0000-0001-7035-1453)

Zlotnik Sergio (Orcid ID: 0000-0001-9674-8950)

Analog and numerical experiments of double subduction systems with opposite polarity in adjacent segments

Mireia Peral[1,2], Jonas Ruh[1,3], Sergio Zlotnik[4], Francesca Funiciello[5], Manel Fernàndez[1], Jaume Vergés[1], Taras Gerya[6]

[1)] Group of Dynamics of the Lithosphere, Institut de Ciències de la Terra Jaume Almera, ICTJA-CSIC, Barcelona, Spain.

[2)] Department of Earth and Ocean Dynamics, Universitat de Barcelona, Barcelona, Spain.

[3)] Structural Geology and Tectonics Group, Geological Institute, Department of Earth Sciences, ETH Zurich, Switzerland.

[4)] Department of Civil and Environmental Engineering, Universitat Politècnica de Catalunya, Barcelona, Spain.

[5)] Laboratory of Experimental Tectonics, Department of Sciences, Università degli Studi Roma Tre, Rome, Italy.

[6)] Institute of Geophysics, Department of Earth Sciences, ETH Zurich, Switzerland.

.

This article has been accepted for publication and undergone full peer review but has not been through the copyediting, typesetting, pagination and proofreading process which may lead to differences between this version and the Version of Record. Please cite this article as doi: 10.1029/2020GC009035

ABSTRACT

In this work we study the dynamics of double subduction systems with opposite polarity in adjacent segments. A combined approach of numerical and analog experiments allows us to compare results and exploit the strengths of both methodologies. High-resolution numerical experiments complement laboratory results by providing quantities difficult to measure in the laboratory such as stress state, flow patterns and energy dissipation. Results show strong asymmetries in the mantle flow that produce in turn asymmetries in the trench and in the downgoing slab deformation. The mantle flow pattern varies with time; the toroidal cells between the plates evolve until merging into one unique cell when the trenches align. In that moment the maximum upward flow is observed close to the trenches. The interaction between the mantle flow produced by each subducting plate makes the rollback processes slower than in a single subduction case. This is consistent with the observed energy dissipation rate that is smaller in the double subduction system than in two single subductions. Moreover, we provide a detailed analysis on the setup and boundary conditions required to numerically reproduce the analog experiments. Boundary conditions at the bottom of the domain are crucial to reproduce their analog counterparts. Numerical results are compared to natural examples of multi-slab subduction systems in terms of upper mantle seismic anisotropy, relative trench-retreat velocities and composition of subduction-related magmatism.

Keypoints

- Numerical models of double subduction have been developed to reproduce laboratory experiments and to understand the dynamics of the system.
- The interaction between the induced mantle flows slows down the evolution of the system and generates additional deformation of plates.
- In the horizontal plane mantle flow forms four toroidal cells with symmetry axes that rotate during trench retreat.

Keywords: mantle flow/plate interaction, numerical and analog models, trench retreat, trench curvature, plate deformation

1 INTRODUCTION

The study of subduction zones is of prime importance since they play an essential role as main driving mechanism for plate tectonics and mantle dynamics [*Coltice et al.*, 2019]. A large part of the current subduction zones, where a single oceanic plate descends beneath another continental or oceanic plate, are associated with nearly linear trenches that extend over distances of some thousands of kilometers (e.g., Aleutians, Peru-Chile, Kermadec-Tonga, Japan–Kurile, Java–Sunda). Mantle dynamics in such subduction zones is dominated by poloidal cells induced by the entrained flow beneath the slab and the corner flow produced by the down dip of the slab. Toroidal cells around the slab edges can be developed in response to the return mantle flow associated with the trench migration [*Gable et al.*, 1991].

This mantle flow pattern can be largely modified by the presence of vertical and horizontal slab tears and slab fragmentation [e.g., *Liu and Stegman*, 2012; *Long*, 2016; *Magni et al.*, 2017]. Furthermore, in settings where oceanic plates are highly segmented, subduction is commonly characterized by very arcuate trenches of limited extent showing different slab dip orientations. Indeed, we can observe double subduction systems with parallel trenches with inward-dipping polarity as in Luzon [*Bautista et al.*, 2001], outward-dipping polarity as in Molucca Sea [*Zhang et al.*, 2017], or same-dipping polarity as in Philippine Sea [*Faccenna et al.*, 2018]. In addition, there are subduction systems characterized by two adjacent slabs retreating in opposite directions as in Taiwan [*Lallemand et al.*, 2001], New Zealand [*Lamb*, 2011], the Western Mediterranean [*Vergés and Fernàndez*, 2012] and the Alps-Apennine junction in Italy [*Vignaroli et al.*, 2008]. All these complex subduction systems can modify the sub-lithospheric mantle flow generating seismic anisotropy and the geochemical signature of subduction-related magmatism [e.g., *Faccenda and Capitanio*, 2013; *Ma et al.*, 2019; *Magni*, 2019].

The dynamics of double subduction systems have been investigated by a wealth of numerical and analog experiments involving different configurations [e.g., *Di Leo et al.*, 2014; *Holt et al.*, 2017; *Mishin et al.*, 2008*; Pusok and Stegman, 2019*]. In particular, subduction systems characterized by two adjacent slabs retreating in opposite directions have been tested with 3D numerical [*Király et al.*, 2016] and analog experiments [*Peral et al.*, 2018]. Whereas *Király et al*. [2016] focused on the interactions between the return flows generated by the respective retreating slabs, *Peral et al*. [2018] investigated plate deformation and variations in trench retreat velocities. Although both models use similar geometries and share main outcomes, differences in the model setup make it difficult to compare them.

Combining computational and laboratory models of the same geodynamic process may help understanding its dynamic evolution by complementing each method's weaknesses and strengths [e.g., *Mériaux et al.*, 2018; *Panien et al.*, 2006]. While laboratory experiments provide the physical realism and high temporal and geometrical resolution, numerical models allow for fully controlling and quantifying physical parameters, as velocity and stress, which cannot be directly obtained from laboratory experiments. This said, the numerical reproduction of laboratory results in terms of temporal evolution of the subduction process, trench curvature, and slab geometry helps identifying and understanding boundary conditions, rheological behavior and other effects in analog experiments.

Only a couple of studies compare analog and numerical experiments of single-plate subduction and elaborate differences and similarities obtained by the different methods [*Mériaux et al.*, 2018; *Schmeling et al.*, 2008]. *Schmeling et al.* [2008] pointed out the importance of a zero-density weak top layer to simulate the free surface behavior when trying to reproduce laboratory experiments numerically. More recently, *Mériaux et al.* [2018] presented 3D numerical models with the objective of reproducing single-plate subduction laboratory experiments. They proposed

that surface tension effects of the syrup representing the mantle material in analog experiments may affect the resulting trench retreat velocity and flank stability of subducting plates.

Here, we perform numerical models aiming to reproduce analog experiments of complex double subduction systems as recently published in *Peral et al.* [2018]. In this regard, the geometrical setup and material parameters have been chosen to best represent values applied in the laboratory. The main objective of our work is to better understand the evolution of small-scale subduction systems with opposite polarity in adjacent segments by determining the relevant physical parameters that characterize these processes. The study is divided into three main objectives: 1) Testing the effects of boundary conditions, rheology and plate thickness on the evolution of single- and double-plate subduction systems to evaluate how the assumed simplifications in numerical models can affect the results. Furthermore, those results also help to identify the nature of analog boundary conditions and rheological uncertainties. 2) Establishing a reference subduction system with opposite polarity to analyze plate deformation and mantle flow interaction by quantifying velocities, stresses and forces within such systems. 3) Comparing numerical results to natural systems and interpreting the geological consequences during the evolution of these subduction systems in terms of trench retreat velocities, plate deformation, magmatism, and seismic anisotropy.

2 METHODOLOGY

2.1 Analog model

Laboratory experiments presented by *Peral et al.* [2018] were performed in a plexiglass tank with dimensions of 150 x 150 x 50 cm^3. Materials consist of both linear viscous glucose syrup and silicone putty representing the upper mantle and subducting plates, respectively. Subduction

is driven by a density difference between the initially floating plates and the mantle material. All material parameters and respective scaling are described in Table 1. Among the models included in *Peral et al.* [2018] we have chosen the double subduction configuration consisting of 10 cm wide plates, and the single subduction configuration with a 30 cm wide plate for comparison to numerical experiments. The length of the plates (l) measures 30 cm and the distance between the trailing edges (s) is 39 cm (Fig. 1). The plates are fixed at their trailing edge and the upper/lower mantle boundary is simulated by placing a fixed base at 11 cm depth. Subduction is initiated by manually pushing down the leading edge of the plates into the syrup to about 3 cm depth. For more details about the analog experiments, we refer to *Peral et al.* [2018].

2.2 Numerical model

The numerical counterparts of single plate and double plate subduction models with opposite polarity have been performed by a three-dimensional code based on the finite difference method with a fully-staggered Eulerian grid and freely advecting Lagrangian markers [*I3ELVIS*; *Gerya*, 2009; *Gerya and Yuen*, 2007]. Similar to the analog experiments we applied a linear (Newtonian) rheology. The numerical model solves the equation for conservation of mass assuming incompressibility

$$\frac{\partial v_i}{\partial x_i} = 0 \qquad (1)$$

and conservation of momentum (Stokes equation)

$$\frac{\partial \tau_{ij}}{\partial x_j} - \frac{\partial P}{\partial x_i} = \rho g_i \qquad (2)$$

where v_i are the velocities in x-, y- and z- direction, x_i are the spatial coordinates, P is the dynamic pressure, ρ is the density, and g_i is the gravitational acceleration. Deviatoric stresses are defined by

$$\tau_{ij} = \eta\left(\frac{\partial v_i}{\partial x_j} + \frac{\partial v_j}{\partial x_i}\right) \quad (3)$$

where η denotes the viscosity.

The governing equations are solved with an OpenMP-parallelized multigrid solver running on 16 threads. The duration of single time steps is capped to ensure that no marker moves further than 1/10 of a nodal cell size, with a maximal value of one minute (average time steps defined by marker movement are around four seconds). Numerical experiments needed around two weeks to complete. Respectively, wall time of conducted experiments average out at around 5400 hours (runtime multiplied by amount of threads). The nodal resolution of the models depends on the size of the computational domain (Table 2). All experiments initially contain eight Lagrangian markers per nodal cell. Marker properties are interpolated to nodes by an arithmetic averaging scheme, whereas the velocity field calculated on the Eularian grid is back-interpolated onto the markers by applying the fourth-order Runge-Kutta method.

Model setup

Geometrical and physical parameters of numerical models have been chosen to best reproduce analog experiments from which we have selected those with narrow plates in the double subduction system and wide plates for the single plate system. All experiments with only one plate exhibit a vertical plane of symmetry parallel to the subduction direction in the middle of the plate. Technically, these experiments could have been conducted in a half space. However, we decided to apply full box sizes for all experiments for a better visual comparison to analogue and asymmetric numerical experiments. To assess boundary effects acting on the subduction system, three Eulerian box sizes have been considered since the smaller the size of the box, the higher the numerical resolution. Large, intermediate and small boxes measure 150 x 150 cm^2 (model N1), 80 x 80 cm^2 (model N2) and 30 x 40 cm^2 (model N3) in horizontal directions, respectively. The

largest box model corresponds to the real dimensions of the tank used in the laboratory experiment [*Peral et al.*, 2018]. Due to the relatively large cell size in model N1, plates are initially spaced 2 cm while in the rest of the models the initial lateral distance is of 1 cm, corresponding to the separation that is observed in the laboratory experiments immediately after subduction initiation. All models have a height of 12 cm. The initial distribution of markers is characterized - from bottom to top - by 11 cm of mantle and 1 cm of "sticky-air", which is a low-density, low-viscosity phase imposing low shear stresses along its interface with the mantle/plate and allowing the system to develop a surface topography. The top boundary of the sticky-air layer is no-slip. We have also tested models with free-slip top boundary conditions showing very similar results though consuming a much longer computation time.

The density of the mantle material is 1445 kg/m^3, the plates have a density of 1505 kg/m^3 and the "sticky-air" layer has a density of 1 kg/m^3 (Table 2). All models but one exhibit a linear viscous rheology for both plates and mantle (Table 2). Plates have an initial thickness of 1 cm, 1.2 cm or 1.35 cm and are located at the top of the mantle, in contact with the "sticky-air" layer (Fig. 1). Plate lengths are 30 cm with a width of 10 cm for double plate and a width of 10 cm or 30 cm for single-plate models (Table 2). Plates are fixed at their trailing end by predefined null nodal velocity in all directions at a distance of 39 cm to each other parallel to the plate extent (Fig. 1). To initiate density-driven subduction, a small slab perturbation is initially imposed at their tips where the slab penetrates 3 cm into the mantle at 45° dip angle. One additional model has been conducted with a non-linear, strain-rate dependent viscosity for the subducting plate (model N15). The non-linear viscosity is calculated by

$$\eta_l = \eta_0 \cdot \dot{\varepsilon}_{II}^{\left(\frac{1}{n}-1\right)} \qquad (4)$$

where η_0 denotes the reference viscosity, n is the power-law exponent and $\dot{\varepsilon}_{II}$ the second invariant of the strain-rate tensor (Table 2).

188 Subduction of the plate(s) in the numerical models is dynamically self-consistent in the sense
189 that it is driven by density contrast only and no material flux is allowed into and out of the model
190 domain. Lateral and bottom boundary conditions are variably prescribed as no-slip or free-slip
191 (zero shear stresses along boundary) to test their effect on mantle flow and subduction retreat
192 (Table 2).
193

194 **3 COMPARING ANALOG - NUMERICAL EXPERIMENTS**

195 Preliminary numerical models have been run reproducing the laboratory conditions to better
196 understand how the numerical/analog modeling constraints affect the final results in the natural
197 prototype rather than to the laboratory experiments itself. A 3-steps parametric study has been
198 performed allowing to design the optimum numerical experiment to study the double subduction
199 systems: First, numerical models of double subduction systems with 10 cm wide plates were
200 designed to test the effects of variable model domain size. Second, the importance of applied
201 numerical boundary conditions was investigated. Finally, numerical models with a single 30 cm
202 wide plate were conducted to reveal the effects of plate stiffness by varying plate viscosity and
203 thickness. Geometric and physical parameters of all presented models are listed in Table 2.

204 Results are described taking into account the different phases of the evolution of a subduction
205 system with opposite polarity in adjacent segments described in *Király et al.* [2016]: i) initial
206 stage corresponding to the evolution of the system until plates reach the base of the upper mantle
207 (phase 1); ii) approaching trenches, starting with the acceleration of slab rollback after the slabs
208 interact with the lower mantle and finishing when trenches intersect, i.e. are aligned to each other
209 (phase 2); and iii) diverging trenches, spanning from trench intersection until subduction
210 completes (phase 3). We define trench intersection as the transition from phase 2 to phase 3.

3.1 Influence of model domain size

Numerical models with different box sizes show similar plate geometries during the different phases of subduction (Fig. 2). Phase 1 is not shown in this section as the trenches are too far from each other to produce any interaction between plates. Phase 2 shows that plates tend to approach each other, this effect being more intense for the medium and small box experiments. In phase 3, subduction continues and the slabs show a flattened asymmetric shape lying on the bottom of the model. This asymmetric deformation is less intense in model N1, where plates are initially more separated. The flow pattern at 6 cm depth from the top of the model domain is similar in all models (Fig. 2), though the radius of the toroidal flow is smaller as the box size decreases. The maximum mantle velocities (~1.4 mm/min) at this depth are registered in front of the trench and behind the slab during the entire subduction process.

Figure 3 illustrates the amount of trench retreat versus time for numerical experiments with different box sizes in comparison to the reference analog experiment. Trenches of the analog experiment retreat with a roughly linear trend (orange and black points in Fig. 3 with their linear regression as black line). In contrast, curves of numerical experiments show a concave trend indicating a slight acceleration during phase 3 that is most evident in model N2 (80 x 80 cm^2) (Fig. 3).

3.2 Influence of applied boundary conditions

We first analyze the role of the conditions applied to the lateral boundaries of the model domain. Figure 4 illustrates the temporal evolution of trench retreat of models with free-slip (N1, N2 and N3) and no-slip (N4, N5 and N6) conditions. Applying free-slip conditions allows the mantle material to move along the lateral walls of the box without resistance. Contrariwise, no-slip lateral boundary conditions prevent lateral flow on the surface of the walls. There are no noticeable differences in the resulting trench retreat related to these two end-member boundary

conditions for models with box size of 150 x 150 cm^2 and 80 x 80 cm^2. However, models N3 and N6 (box size 40 x 30 cm^2) show a measurable offset with free-slip boundaries resulting in a slightly faster trench retreat (Fig. 4).

Secondly, we explore the effects of applying a free-slip or no-slip boundary condition at the bottom of the model domain (Fig. 5). Laboratory experiments show that subducted plates when reaching the basal plate, at least to a certain extent, deform and move horizontally. This observation requires testing different bottom boundary conditions for the numerical counterpart [*Peral et al.*, 2018]. A double subduction model with no-slip boundary condition at the bottom implies zero horizontal velocity for the mantle and the slab material at the base of the model domain. Therefore, lateral movement and stretching of the plate lying on the floor of the model is restricted (Fig. 5a). On the other hand, free-slip boundary conditions at the bottom allow the slabs to stretch in horizontal directions and slabs can move laterally along the bottom boundary depending on the resulting velocities (Fig. 5b). Trench retreat velocities are up to 15% higher for free-slip than for no-slip conditions and the toroidal mantle flow produces a lateral movement of both slabs that is not observed for the no-slip models.

3.3 Influence of plate rheology and plate thickness

Previous laboratory experiments of single and double subduction have shown that the trenches of subducting plates exhibit a more intense curvature than numerical models when applying the measured spatial and rheological parameters (Fig. 6a, 6b). This effect, which is more pronounced for wider plates, raises the question whether the rheology of the plates and the mantle differ for laboratory and numerical models. Therefore, a series of numerical models with a 30 cm wide single plate was conducted to test the effects of plate rheology and thickness on the subduction process and particularly on the trench curvature (see Table 2 and Fig. 6).

Results show that the trench curvature, defined as the ratio between the chord and the sagitta of the circular segment delineated by the trench [*Peral et al.,* 2018], decreases and the deformation and stretching of the slab increases with a decreasing viscosity ratio between the lithosphere and the mantle ($\gamma = \eta_l/\eta_m$). Reducing the viscosity ratio from a reference value γ = 195 to γ = 100 is not sufficient to reproduce the slab deformation observed in the laboratory experiment (Fig. 6c). However, reducing at the same time the viscosity ratio to γ = 100 and the plate thickness to 1.2 cm maintains the trench curvature showing a more pronounced slab deformation (Fig. 6d). A similar effect has been observed for a non-Newtonian plate viscosity (Fig. 6e). The numerical model that best represents the laboratory experiment in terms of plate deformation (slab deformation and trench curvature) is obtained by reducing the plate thickness to 1.0 cm (Fig. 6f). However, the time evolution of this model (model N11) differs notably from that performed in the laboratory.

3.4 Reference model for the double plate numerical experiment

Reducing the computational domain allows to increase the model resolution without increasing the computational cost and therefore to simulate the laboratory experiment with more spatial accuracy. Regarding the size of the computational domain, negligible differences in terms of plate geometry and trench retreat velocity are obtained when reducing the numerical domain from 150 x 150 cm^2 to 80 x 80 cm^2 and 40 x 30 cm^2 for 10 cm wide plates (Fig. 2, 3). In terms of trench retreat the numerical model that best matches the laboratory experiment is model N3 (40 x 30 cm^2), which allows the highest resolution (Table 2). However, the toroidal flow for this model is narrower than for the medium and large models, due to the proximity of the lateral walls to the slabs. Indeed, the effect of applied free-slip or no-slip lateral boundary conditions on trench retreat velocity is only noticeable for the small-box numerical experiments, indicating undesired boundary effects (Fig. 4). Furthermore, velocity magnitudes at the lateral walls of free-slip

experiments of the small box model N3 are significantly larger than for models N1 and N2 (Figure S1).

The bottom boundary condition strongly affects the slab geometry (Fig. 5). The slab deformation and temporal evolution of the subduction system observed in the laboratory experiment is better reproduced by numerical models having no-slip boundary conditions at the bottom of the model domain.

The important effect of rheology and plate thickness on plate deformation is evident from the results obtained from numerical models of single subduction with 30 cm wide plates (Fig. 6). The model with non-linear viscosity plate (model N15; Fig. 6e) shows the most acceptable similarity with the laboratory experiment in terms of plate deformation and time evolution, indicating that the materials used in the laboratory may be not perfectly linear viscous. On the other hand, changing the plate thickness or the linear viscosity contrast between plate and mantle strongly affects the temporal evolution of the subduction system (Fig. 6).

Following the above discussed results, to study the evolution of subduction processes with opposite polarity in adjacent segments, we choose a reference numerical setup exhibiting a medium box size (80 x 80 cm^2) with boundary conditions of free-slip at the lateral walls and no-slip at the bottom of the model domain (model N2; see Table 2). We chose this model because it shows the best trade-off between numerical resolution, trench curvatures, deformation of plates and trench retreat velocities. The differences observed in the trench retreat vs. time between model N2 and the analog experiment (Fig.3) can be explained by the larger trench curvature and the slab friction with the bottom boundary exhibit by the analog model, which consumes more energy slowing down the process.

4 NUMERICAL MODEL OF SUBDUCTION WITH OPPOSITE POLARITY IN ADJACENT SEGMENTS

In the following, we present the results obtained from the numerical model N2 consisting of two 10 cm wide plates with an initial separation of 1 cm (Table 2). The interaction between both plates is investigated by analyzing (1) mantle flow, (2) stress and energy dissipation, (3) plate deformation and (4) trench retreat velocity. Results are compared with those from a numerical model of single-plate subduction (model N8) and the respective double subduction laboratory experiment (model L1, Table 2).

4.1 Mantle flow

The mantle velocity field induced by the double plate subduction process is calculated at different times and depth levels and entirely presented in the Supporting Material (Figs. S2-S5). Figure 7 shows the three-component velocity field at 6 cm depth of the model domain corresponding to intermediate mantle depths with the magnitude-less horizontal mantle flow direction in the background. At 65 min, mantle flow exhibits a rotational symmetry of second order with the rotation point at the center of the model (Fig. 7; top row). This symmetry pattern is also observed through the whole evolution of the system, which is characterized by four large toroidal cells with flows converging towards the front-side of the trenches and diverging outwards from the backside of the trenches. The symmetry axes of the cells are roughly orthogonal and rotate counterclockwise through the different phases as a result of the progressive trench retreating (Fig. 7). The orientation of these axes, as well as the size of the cells and its symmetry, depends on the initial geometry of the system (plate width, plate separation, and box size). In our experiment, during phases 1 (from minute 0 to 53), phase 2 (from minute 53 to 102) and early phase 3 (from minute 102 to 140), the induced toroidal mantle flow is asymmetrical with respect to the longitudinal axis (*x*-direction) of each plate, particularly in the back-side of

329 the trenches (see also Fig. 9). The two toroidal cells around the adjacent lateral slab edges push
330 the plates towards each other and merge into a single cell during trench intersection. During late
331 phase 3 (>140 min), the interaction between the adjacent plates vanishes and the toroidal flow
332 cells become nearly symmetrical in the back-side of the trenches but strongly asymmetrical in
333 the front-side (Fig. 7).

334 The velocity component v_z, parallel to the initial subduction trenches, is the most affected by the
335 interaction between the two plates (Fig. 7a). During phase 2, this component is stronger at the
336 external backside of the slabs because the inner toroidal cells associated with the return flow
337 around the slab have opposite directions in the inter-plate region. Merging of the two inner
338 toroidal cells is observed through the trench-parallel vectors in the inter-plate region during plate
339 intersection. When slabs cross each other at 6 cm depth this component becomes stronger in the
340 inter-plate region reaching its maximum absolute values (±1.1 mm/min). As phase 3 progresses,
341 maximum values of v_z component are observed at the outer front side of the slabs. In contrast, the
342 v_x component shows roughly the same pattern during the entire evolution, being higher in front
343 of the slabs (Fig. 7b). The vertical velocity component v_y at intermediate mantle depths shows
344 upwelling around the plates, compensating for the plates' descendence. An exception is the inter-
345 plate region, where mantle material is dragged down locally during trench intersection (Fig. 7c).

346 Figure 8 shows the mantle flow of model N2 in three dimensions during trench intersection (Fig.
347 8a) and the evolution of the velocity field along a cross-section through one of the subducting
348 plates (Fig. 8b). The circulation in front and behind the slab is mostly poloidal incorporating the
349 mantle material displaced by both plates in a vertical plane. Maximum upward velocities occur
350 during phase 1 (time evolution <65 min) in front of the slab persisting through all the process but
351 with a lower intensity. During phase 2 (from minute 53 to 102) there is a noticeable upward
352 velocity component affecting the region behind the slab that is vanishing along phase 3. In the
353 inter-plate region, the mantle material flows upwards associated with the front side of the slabs

(Fig. S5). These upwelling flows approach each other as the subduction progresses changing during trench intersection when upwelling is associated with the backside of the slabs. During intersection, the mantle flow in the inter-plate region changes direction generating a downward vertical flow that is not observed in other regions of the mantle or during other phases (Figs. 7c and S2-S5).

4.2 Stress and energy dissipation

A different way to figure out how plates interact with each other through the generated mantle flow is analyzing the stress distribution and the total energy dissipated during the subduction process. Figure 9 shows the second invariant of the stress tensor $\sigma_{eff} = \left(\frac{1}{2} * [(\sigma_1 - \sigma_2)^2 + (\sigma_1 - \sigma_3)^2 + (\sigma_2 - \sigma_3)^2]\right)^{1/2}$ calculated at intermediate mantle depth (6 cm from the top of the model domain) and the direction of the horizontal velocity field. At this depth, stress values of 0.6 Pa are registered in the mantle regions adjacent to the slabs during the entire subduction process. However, as the subduction progresses, the stress increases from 0.05 Pa to more than 0.2 Pa in the vicinity of the internal sides of the slabs reaching maximum values (> 0.45 Pa) in the inter-plate region during the trench intersection. In the course of phase 3, the mechanical coupling vanishes progressively.

Additionally, we have calculated and compared the energy rates dissipated $dW = V \cdot dt \cdot \dot{\varepsilon}_{ij} \cdot \tau_{ij}$ by the mantle of both single- and double plate subduction models as shown in Figure 10. In the double subduction model, the maximum rate of energy dissipation occurs during phase 1 reaching ~$1.2 \cdot 10^{-6}$ W, before the slabs reach the base of the box when energy dissipation rate decays rapidly to ~$0.3 \cdot 10^{-6}$ W (Fig. 10; red line). During phase 2, the energy dissipation rate increases again until $0.9 \cdot 10^{-6}$ W before it decreases to a stable value of ~$0.7 \cdot 10^{-6}$ W. From minute 150 on to the end of subduction (minute 200) there is a steady increase in energy

dissipation rate up to $0.9 \cdot 10^{-6}$ W (Figure 10; red line). The dissipated energy rate for the single-plate model (model N8) shows a similar pattern with values that are slightly larger than half of those calculated for the double plate model (Fig. 10; grey line). Indeed, the total dissipated energy calculated for a single plate (0.0044 J) is half of that corresponding to a double plate system (0.009 J) considering 200 minutes of evolution in both cases. This released energy represents ~16% of the total potential energy of the system, the rest being partly held as potential energy as plates are still subjected to their trailing edges, and partly being dissipated by plate deformation.

4.3 Plate deformation

To visualize plate deformation during the double subduction process corresponding to model N2, we illustrate the mantle velocity field at 1.2 cm depth from the top of the model domain, i.e. 2 mm into the plates from the sticky-air interface (Fig. 11), and the second invariant of the strain rate within the two plates (Fig. 12). The velocity field observed at the plate level indicates that, from the beginning of the experiment until early phase 3, the mantle flow pushes the plates towards each other in a direction perpendicular to their respective longitudinal axes producing a lateral movement of both plates (Fig. 11). This is also observed in Fig. 12 in which strain rate increases from the center of the plates to their borders as a result of lateral movement. Trenches show a symmetric curvature that slightly decreases with time accompanied of a counter clockwise rotation due to the lateral movement of plates (Figs. 11, 12). As expected, the highest strain rates occur in the regions where plates bend vertically, i.e. near the trenches and at the bottom of the model where plates get horizontal.

4.4 Trench retreat velocity

Figure 13 shows the time evolution of trench retreat velocity for single- and double-plate subduction systems. In the double subduction model, trench retreat velocities of both plates are

roughly equal due to the symmetry of the initial setup (minor differences may occur related to the technique of trench localization which is also dependent on random marker distribution). Phase 1 is characterized by a fast trench retreat until ~40 min, followed by a velocity decrease until the tips of the plates reach the base of the model box at around 53 min (Fig. 13). During phase 2, trench retreat velocity increases again reaching a maximum of ~1.6 mm/min followed by a short period of velocity decrease before trenches intersect at around 102 min. Phase 3 is characterized by a progressive increase in retreat velocity reaching maximum values of ~1.9 mm/min at the late stage of evolution. The single plate model (model N8) shows similar trench retreat velocity variations during all phases of the subduction process although is slightly faster reaching a maximum velocity of ~2.1 mm/min during phase 1 (Fig. 13). The higher speed computed in the single plate model relative to the double plate model is consistent with the calculated energy dissipation rate, which is slightly higher than half of that for the double plate model (Fig. 10). As the total energy is exactly half, the time over which the energy rate is integrated must be lower and therefore, the velocity faster.

5 DISCUSSION

In the following, numerical results are discussed with respect to the three main objectives introduced earlier, which include 1) testing the effects of rheology and boundary conditions and compare them to laboratory experiments in terms of temporal and structural evolution, 2) investigating and quantifying mantle flow and plate deformation in a double subduction experiment, and 3) comparing the obtained numerical data to natural cases of double subduction.

5.1. Comparison of numerical and laboratory experiments

Numerically reproducing laboratory experiments is not straightforward. Indeed, other authors already found differences in the sinking and retreating rates and plate morphology when attempting to numerically reproduce laboratory experiments of single-plate subduction [*Mériaux et al.*, 2018; *Schmeling et al.*, 2008]. Performing both models simultaneously helps us to control all the parameters affecting the evolution of the system. The agreement between results from numerical and laboratory models is fairly good when considering an intermediate domain size (80 x 80 cm^2) with free-slip boundary conditions for the lateral sides and no-slip at the bottom of the numerical model, although the effect of applying different lateral boundary conditions is weak. First-order observations like temporal evolution of subduction, plate and trench geometries, plate deformation and mantle flow are similar in both models (Figs. 2 and 12). However, the two methodologies produce also slight differences. For example, the experimental uncertainties related to the handling process of the laboratory experiments can lead to asymmetries between plates in the initial stages of the evolution of the system or to slight modifications in the rheology of materials. Nevertheless, we found that these factors, which are complex to quantify, produce only second-order differences.

Aside these differences related to inaccuracies from the experimental handling, there are others related to simplifications made in the numerical approach. For example, the overall slab deformation as well as the temporal evolution of the subduction process is more accurately reproduced when applying no-slip boundary conditions at the bottom of the model domain (Fig. 5). However, the laboratory experiments show that the plates stretch and extend horizontally once lying on the model box floor (Fig. 12), indicating that the analog boundary condition ranges in between those end members (free slip / no slip). An intermediate boundary condition is also expected for the horizon separating the upper from the lower mantle, where an increase in viscosity with a factor of 10 to 100 indicates resistance but does not prohibit viscous drag [e.g., *Király et al.*, 2017; *Goes et al.*, 2017].

448 Furthermore, numerical experiments cannot reproduce simultaneously the large trench curvature
449 and the retreat velocity observed in laboratory experiments, particularly for wide plates, even
450 when varying the rheological parameters (Fig. 6). This points towards potential effects that were
451 not taken into account as the formation of a thin "crystalized" layer at the surface of the syrup,
452 which might generate surface forces not considered in the numerical model [e.g., *Mériaux et al.*,
453 2018].

454 Concerning double subduction systems with opposite polarity, numerical and analog experiments
455 are in general agreement in terms of overall duration of the subduction process. Furthermore,
456 stresses generated in the inter-plate region in both numerical and analog models, tend to separate
457 the plates from each other (Figs. 9, 11; and Fig. 7 in *Peral et al*., 2018). However, some
458 discrepancies between the results of the two modeling approaches should be discussed in more
459 detail: Analog experiments show a divergent displacement of the two plates, whereas in
460 numerical experiments the resulting deformation of plates shows a lateral movement that brings
461 the central parts of the plates closer together (Figs. 11, 12). This discrepancy can be explained by
462 the different radii of the toroidal cells generated in both experiments, which seems to be larger in
463 the numerical than in the analog models independently on the size of the modeling domain (Fig.
464 2). Another discrepancy is observed related to trench retreat velocities. Laboratory experiments
465 show retreat velocities increasing until plate intersection and decreasing thereafter [*Peral et al.*,
466 2018], whereas velocities remain roughly constant or even increase towards the end of the
467 subduction process for numerical experiments (Fig. 3, 13). A possible explanation are the
468 different mantle flow patterns and associated evolution of energy dissipation (Fig. 10) that are
469 affected by implemented boundary conditions in numerical models and experimental
470 uncertainties in the analog setup, as well as different rheological properties between analog and
471 numerical materials. Concerning the shapes of subducting plates, asymmetric trench curvatures
472 are observed in both numerical and laboratory experiments suggesting that these asymmetries are

related to the mantle flow interactions associated with double subduction systems (Fig. 12). A more detailed study of the mantle flow in analog experiments is needed to better understand the observed differences.

5.2. Dynamics of double subduction systems

Mantle flow in an ideal single-slab subduction system is characterized by a toroidal component that is symmetric relative to the longitudinal axis of the slab. In the case of two adjacent slabs with opposite polarity, the toroidal flows induced by both slabs interact with each other generating different flow patterns in the inter-plate and outer mantle regions. Consequently, the resulting toroidal component of the mantle flow becomes asymmetric relative to the slabs axes (Figs. 7, 11). This asymmetry prevents for applying a half-space model domain as for example in *Kiraly et al*. [2016], whose setup implies an indefinite repetition of slabs laterally by introducing free-slip side boundaries cutting the opposite polarity slabs. Such boundary conditions are strictly valid for plates exceeding 1000 km width or for tectonic scenarios where the opposed polarity repeats several times. In any case, the resulting flow pattern has important implications for subduction driven by rollback, where the toroidal flow makes up 95–100% of the entire mantle flux [*Schellart et al.*, 2007]. For example, assuming that seismic anisotropy in the upper mantle is related to the lattice preferred orientation of olivine as a result of large-scale mantle flow [e.g., *Silver et al.*, 1996; *Long and Becker*, 2010] allows detecting complex subduction scenarios and understanding related mantle dynamics [*Alpert et al.*, 2013; *Wei et al.*, 2016]. For double subduction systems similar to the ones presented in this study, the orientation of the symmetry axes of the toroidal cells may help interpreting inter-plate coupling and the spatial framework of adjacent trenches (Fig. 7a).

Deformation of plates is coupled to the mantle flow and, therefore, affected by mantle flow asymmetry producing lateral movement of the plates and additional deformation of the slabs in

497 double subduction systems (Fig. 12). The deformation experienced by the plates is related to the
498 mantle drag exerted by the net outward flow separating one plate from the other. The strength of
499 this drag decreases with the distance between the slabs, so its effect is maximum during the
500 intersection of the two trenches. Similar behavior has been reported by *Király et al.* [2016]. The
501 interaction between the flows generated by the two slabs reduces the energy dissipation rate
502 compared to two isolated plates. As a consequence, the trench retreat velocities in a double
503 subduction system are slowed down with respect to a single subduction process. An exception is
504 the end of phase 3 (t >150 min), where plates are sufficiently far from one another and trench
505 retreat is accelerating rather than keeping a constant velocity as in the case of a single plate
506 subduction (Figs. 10, 13).

507 Despite the strong interaction between plates in a double subduction system, the evolution of the
508 trench velocity through time shares some common features with the single subduction system.
509 Obviously, these similarities are stronger during the initial and final stages of the evolution,
510 when the two slabs are distant and the interaction of their induced mantle flows is weaker. For
511 example, as reported elsewhere [*Funiciello et al.*, 2003; *Funiciello et al.*, 2006; *Schellart*, 2004;
512 *Strak and Schellart*, 2014], trench velocity increases rapidly at the beginning of the model whilst
513 the slab is sinking and the negative buoyancy increases (Fig. 13; 0 to ~40 min). When the slab
514 reaches the bottom of the domain (40 to 55 min), the trench velocity slows down and accelerates
515 again (from 55 to 75 min) until the steady-state subduction is achieved (75 to 180 min). During
516 the steady-state period, the single subduction system shows some minor periodic accelerations
517 and decelerations probably due to changes in the slab angle (Fig. 13). These changes are not so
518 evident in the double subduction system as the interaction between slabs and mantle flow is
519 probably overprinting the slab dip changes.

520 **5.3 Relevance for natural prototypes**

Complex subduction systems formed by several slabs, with reduced dimensions and with advancing or retreating trench migration velocities, can produce changes in the stress, strain rate, and pressure and temperature conditions in the mantle modifying the lattice preferred orientation of olivine crystals and seismic anisotropy as manifested by shear-wave splitting [*Faccenda*, 2014; *Faccenda and Capitanio*, 2013]. Similarly, the incorporation of sediments and hydrous fluids into the sub-lithospheric mantle during subduction and the rise of the asthenosphere through slab tears or in the backarc extensional basins can result in volcanic activity with a variety of geochemical signatures [e.g., *Lustrino et al.*, 2011; *Melchiorre et al.*, 2017].

As mentioned in the introduction, natural prototypes where double subduction systems with opposite polarity in adjacent segments have been proposed to occur have been identified in Taiwan, New Zealand, the Western Mediterranean and the Alps-Apennine junction, among others. However, extracting conclusions applicable to these natural scenarios is not straightforward as the presented study is based on oversimplified models of double subduction systems. Main limitations are the lack of overriding plates, the assumption of a viscous rheology for the lithosphere and upper mantle, and the dimensions of plates, which at nature scale are 600 km wide and 1800 km long separated by a 60-120 km wide transform zone. Despite these limitations, we can infer some expected effects derived from the interaction between the plates and the upper mantle in terms of seismic anisotropy and magmatism.

One of the regions where these effects are supported by observations is the Western Mediterranean. There, the Alboran-Tethys and the Algerian-Tethys segments retreated in opposite directions inferred from the present distribution and vergence of the metamorphic complexes in the Betic-Rif and the Tell-Kabylies chains [e.g., *Casciello et al.*, 2015; *Fernàndez et al.*, 2019; *Vergés and Fernàndez*, 2012]. It must be noted that the dimensions of the Ligurian-Tethys domain, whose closure gave rise to the present Western Mediterranean, was narrower

than the slabs modelled in this study, and the trench intersection occurred before the slabs reached the lower mantle (i.e. during phase 1). Fast polarity directions (FPD) inferred from SKS shear wave splitting onshore show a consistent anisotropy pattern oriented parallel to the Betic-Rif orogen [e.g., *Díaz et al.*, 2015; *Miller et al.*, 2013]. Despite the poor coverage of anisotropy data offshore, a regional 3D azimuthally anisotropic model of Europe shows a WSW-ENE alignment of FPD in the Alboran Basin changing to NW-SE in the Algerian Basin at depths of 70 – 200 km [*Zhu and Tromp,* 2013]. At shallower depths however, Pn and Sn tomography shows an almost perpendicular anisotropy pattern for the uppermost mantle with NW-SE oriented FPD in the southern margin of the Alboran Basin varying to NE-SW in the Algerian Basin [*Díaz et al.*, 2013]. These variations in the anisotropy pattern are related to the interaction between the mantle return flows produced by the slabs retreating in opposite directions, the northwest to west displacement of the Alboran-Tethys slab and its tightening, and the absolute motion of the African plate [e.g., *Spakman et al.*, 2018].

The vertical component of mantle flow shows maximum velocities in the back-arc and the inter-plate regions being more active during phases 1 and 2 (Figs. 7 and S2-S5). This mantle upwelling from the deeper parts of the upper mantle can produce widespread melting by adiabatic decompression with variable composition depending on the water content and the depletion degree of the mantle source, which changes spatially with the retreating of slabs as proposed from recent 3D numerical modeling [e.g., *Magni,* 2019]. This variable volcanic geochemical signature is observed in the Western Mediterranean magmatic manifestations changing from tholeiitic in the early Oligocene Malaga dikes to calc-alkaline/HK calc-alkaline and alkaline magmas during Late Miocene to Quaternary. The combination of subduction and rifting events operating in the region produced recycling and depletion of mantle rocks making difficult to associate the derived volcanic products with the present-day geodynamic setting [e.g., *Carminati et al.*, 2012; *Lustrino and Wilson*, 2007; *Lustrino et al.*, 2011; *Melchiorre et al.*,

570 2017]. The limited observations of anisotropy in the offshore regions of the Western
571 Mediterranean, together with the large variety of magmatic compositions, make difficult to favor
572 a unique geodynamic interpretation among those proposed for this region [e.g., *Duggen et al.*,
573 2005; *Faccenna et al.*, 2004; *Platt et al.*, 2013; *Spakman and Wortel*, 2004; *Van Hinsbergen et*
574 *al.*, 2014; *Vergés and Fernàndez*, 2012].

575 Some of the regions where opposed subduction polarity in adjacent plate segments is observed
576 show a strong trench asymmetry with a tight curvature in one of the ends of the trench (e.g.,
577 western Alps, western Betic-Rif, southwest Ryukyu trench). *Kiràly et al.* [2016] proposed that
578 the stress propagation through the mantle produced by the adjacent retreating slabs contributed to
579 the strong curvature of the Western Alps and the SW-Ryukyu trench. However, according to our
580 results, reproducing the arc tightening observed in the above-mentioned regions would require
581 additional 'tectonic' conditions to slow-down or even preventing the slab retreat in one of the
582 plate edges to force the trench curvature.

583 The case of New Zealand where the Pacific plate dips to the west beneath the North Island and
584 the Australian plate dips to the east beneath the South Island is more elusive. The interaction
585 between both slabs is doubtful as they are presently separated by the 500 – 600 km long right-
586 lateral transform fault, which is the critical distance for stress propagation. The curvature of the
587 Hikurangi Trough could be caused by the fast clockwise rotation of the North Island and the
588 collision of the Chatham Rise microplate with the northern part of the South Island [*Wallace et*
589 *al.*, 2009; *Wallace et al.*, 2004]. In addition, the comparison with the presented experiments is
590 hindered because subduction of both plates is not synchronous, initiating 25 Ma in the North
591 Island and 10–12 Ma in the South Island [*King*, 2000; *Schellart et al.*, 2006].

592 Summarizing, the present work allows for identifying some distinctive features related to
593 subduction systems with opposed polarity in adjacent segments. However, its application to

natural prototypes requires a detailed analysis of the tectonic evolution of the study region and the incorporation of a more sophisticated model set-up.

6. CONCLUDING REMARKS

This study presents 3D numerical experiments of subduction systems with opposite polarity of adjacent segments with geometrical and rheological parameters taken from published analog experiments. First, the effects of input parameters such as Eulerian domain size, boundary conditions, and plate geometry and strength were tested and compared to analog results. Second, numerical data was used to better quantify physical processes characterizing the evolution of such double subduction systems and finally for comparison to natural examples.

Comparing numerical to analog experiments allows to conclude:

- The Eulerian domain size has a second-order effect on the overall geometry of plates and the trench retreat velocities during the subduction process. However, elevated velocities along the boundaries of the smallest box setup (30x40 cm^2) indicate that there is a critical small domain size beyond which mantle flow is affected.

- The choice of lateral boundary conditions (free- vs. no-slip) has a minor effect on the subduction process for the intermediate size experiments. For the bottom boundary, a no-slip condition results in plate geometries better comparable to analog experiments, while a free-slip condition moves the bottom-laying plates away from each other.

- The trench retreat evolution of subduction systems (single and double) is reproduced very well with rheological and geometrical input data retrieved from analog experiments. However, the trench curvature values obtained from numerical experiments are smaller than the corresponding analogs. This might be due to uncertainties in the measured

viscosities from analog experiments or spurious deformation of the plates during handling.

- Numerical experiments with thinner and weaker plates can reproduce the trench curvature of analog experiments, but fail in reproducing the trench retreat velocity. This might be due to the crystallization of a fine film on the surface of the syrup.

The physical characterization of double subduction systems and its comparison to natural examples gives the following insights:

- The mantle flow induced by the subduction of adjacent plates pushes the plates against each other. Simultaneously both downgoing slabs and trenches deform asymmetrically and the subduction process evolves slower than the single plate model. During trenches intersection, maximum stresses contribute to further plate deformation.

- In the horizontal plane mantle flow forms four toroidal cells with symmetry axes rotating during trench retreat. The flow lines converge towards the front-side of the trenches and diverge from the backside of the trenches.

- The upward component of mantle flow is maximum around the sinking slabs before the intersection of trenches and decreases as the slabs retreat concentrating around the edges of the slabs after trenches intersection.

- The energy dissipation rate of a plate in a double subduction system is smaller than that of a single subduction. Accordingly, double plate systems exhibit slower trench retreat velocities and a longer duration of the subduction process than a single plate.

- The subduction models with opposite polarity in adjacent segments predict complex patterns of seismic anisotropy, magmatic composition and plate deformation associated with the interaction between the sinking slabs and the surrounding mantle. However, its

application to natural scenarios needs of a more sophisticated model set-up in terms of plates geometry, rheology and incorporation of overriding plates.

Acknowledgements

We are indebted to two anonymous reviewers, the Associated Editor, and the Editor T. Becker for their valuable comments and suggestions that largely improved the previous version of the manuscript. This work is part of the PhD Thesis of MP developed under the projects SUBTETIS-CSIC-201830E039, and AGAUR 2017-SGR-847/2017-SGR-1471. We also thank projects AECT-2018-1-0007 and AECT-2018-3-0007 of the Barcelona Supercomputing Center (BSC-CNS). JR was supported by the Swiss National Science Foundation (grant number 2-77297-15). SZ thank the funding from AGAUR 2017-SGR-1278, the Agencia Estatal de Investigación project DPI2017-85139-C2-2-R and the European Union project H2020-RISE MATHROCKS GA nº 777778. The grant provided to the Department of Science, Roma Tre University (MIUR-ITALY Dipartimenti di Eccellenza, ARTICOLO 1, COMMI 314-337 LEGGE 232/2016) is gratefully acknowledged by F.F. Datasets for this article are available in http://hdl.handle.net/20.500.11850/364963 (DOI: 10.3929/ethz-b-000364963).

References

Alpert, L. A., M.S. Miller, T.W. Becker, and A.A. Allam (2013), Structure beneath the Alboran from geodynamic flow models and seismic anisotropy, *J. Geophys. Res. Solid Earth, 118*, 4265-4277. https://doi.org/doi:10.1002/jgrb.50309.

Bautista, B. C., M. L. P. Bautista, K. Oike, F. T. Wu, and R. S. Punongbayan (2001), A new insight on the geometry of subducting slabs in Northern Luzon, Philippines, *Tectonophysics*, *339*(3-4), 279-310. https://doi.org/10.1016/S0040-1951(01)00120-2.

Carminati, E., M. Lustrino, and C. Doglioni (2012), Geodynamic evolution of the central and western Mediterranean: Tectonics vs. igneous petrology constraints, *Tectonophysics*, *579*, 173-192. https://doi.org/10.1016/j.tecto.2012.01.026.

Casciello, E., M. Fernàndez, J. Vergés, M. Cesarano, and M. Torne (2015), The Alboran domain in the western Mediterranean evolution: The birth of a concept, *Bulletin de la Societe Geologique de France, 186*(4-5), 371-384. https://doi.org/10.2113/gssgfbull.186.4-5.371.

Coltice, N., L. Husson, C. Faccenna, and M. Arnould (2019), What drives tectonic plates?, *Science Advances*, *5*(10). https://doi.org/10.1126/sciadv.aax4295.

Di Leo, J. F., A. M. Walker, Z. H. Li, J. Wookey, N. M. Ribe, J. M. Kendall, and A. Tommasi (2014), Development of texture and seismic anisotropy during the onset of subduction, *Geochemistry, Geophysics, Geosystems*, *15*(1), 192-212. https://doi.org/10.1002/2013GC005032.

Díaz, J., A. Gil, and J. Gallart (2013), Uppermost mantle seismic velocity and anisotropy in the euro-mediterranean region from pn and sn tomography, *Geophysical Journal International*, *192*(1), 310-325. https://doi.org/10.1093/gji/ggs016.

678 Díaz, J., J. Gallart, I. Morais, G. Silveira, D. Pedreira, J. A. Pulgar, N. A. Dias, M. Ruiz, and J.
679 M. González-Cortina (2015), From the Bay of Biscay to the High Atlas: Completing the
680 anisotropic characterization of the upper mantle beneath the westernmost Mediterranean region,
681 *Tectonophysics*, *663*. https://doi.org/10.1016/j.tecto.2015.03.007.

682 Duggen, S., K. Hoernle, P. van den Bogaard, and D. Garbe-Schönberg (2005), Post-collisional
683 transition from subduction-to intraplate-type magmatism in the westernmost Mediterranean:
684 Evidence for continental-edge delamination of subcontinental lithosphere, *Journal of Petrology*,
685 *46*(6), 1155-1201. https://doi.org/10.1093/petrology/egi013.

686 Faccenda, M. (2014), Mid mantle seismic anisotropy around subduction zones, *Physics of the*
687 *Earth and Planetary Interiors*, *227*, 1-19. https://doi.org/10.1016/j.pepi.2013.11.015.

688 Faccenda, M., and F.A. Capitanio (2013). Seismic anisotropy around subduction zones: Insights
689 from three-dimensional modeling of upper mantle deformation and SKS splitting calculations.
690 *Geochemistry, Geophysics, Geosystems. 14.* 243-262. https://doi.org/10.1002/ggge.20055.

691 Faccenna, C., C. Piromallo, A. Crespo-Blanc, L. Jolivet, and F. Rossetti (2004), Lateral slab
692 deformation and the origin of the western Mediterranean arcs, *Tectonics*, *23*(1), TC1012 1011-
693 1021. https://doi.org/10.1029/2002TC001488.

694 Faccenna, C., A. F. Holt, T. W. Becker, S. Lallemand, and L. H. Royden (2018), Dynamics of
695 the Ryukyu/Izu-Bonin-Marianas double subduction system, *Tectonophysics*, *746*, 229-238.
696 https://doi.org/10.1016/j.tecto.2017.08.011.

697 Fernàndez, M., M. Torne, J. Vergés, E. Casciello, and C. Macchiavelli (2019), Evidence of
698 segmentation in the iberia–africa plate boundary: A jurassic heritage?, *Geosciences*
699 *(Switzerland)*, *9*(8). https://doi.org/10.3390/geosciences9080343.

Funiciello, F., C. Faccenna, D. Giardini, and K. Regenauer-Lieb (2003), Dynamics of retreating slabs: 2. Insights from three-dimensional laboratory experiments, *Journal of Geophysical Research B: Solid Earth*, *108*(4), ETG 12-11 - 12-16. https://doi.org/10.1029/2001JB000896.

Funiciello, F., M. Moroni, C. Piromallo, C. Faccenna, A. Cenedese, and H. A. Bui (2006), Mapping mantle flow during retreating subduction: Laboratory models analyzed by feature tracking, *Journal of Geophysical Research: Solid Earth*, *111*(3). https://doi.org/10.1029/2005JB003792.

Goes, S., R. Agrusta, J. van Hunen, and F. Garel, Subduction-transition zone interaction: A review. *Geosphere 13* (3): 644–664. https://doi.org/10.1130/GES01476.1.

Gable, C. W., R. J. O'Connell, and B. J. Travis (1991), Convection in three dimensions with surface plates: Generation of toroidal flow, *Journal of Geophysical Research: Solid Earth*, *96*(B5), 8391-8405. https://doi.org/10.1029/90JB02743.

Gerya (2009), *Introduction to numerical geodynamic modelling*, 1-345 pp. https://doi.org/10.1017/CBO9780511809101.

Gerya, and Yuen (2007), Robust characteristics method for modelling multiphase visco-elasto-plastic thermo-mechanical problems, *Physics of the Earth and Planetary Interiors*, *163*(1-4), 83-105. https://doi.org/10.1016/j.pepi.2007.04.015.

Holt, A. F., L. H. Royden, and T. W. Becker (2017), The dynamics of double slab subduction, *Geophysical Journal International*, *209*(1), 250-265. https://doi.org/10.1093/gji/ggw496.

King, P. R. (2000), Tectonic reconstructions of New Zealand: 40 Ma to the Present, *New Zealand Journal of Geology and Geophysics*, *43*(4), 611-638. https://doi.org/10.1080/00288306.2000.9514913.

722 Király, Á., F. A. Capitanio, F. Funiciello, and C. Faccenna (2016), Subduction zone interaction:
723 Controls on arcuate belts, *Geology*, *44*(9), 715-718. https://doi.org/10.1130/G37912.1.

724 Király, Á., F. A. Capitanio, F. Funiciello, and C. Faccenna (2017), Subduction induced mantle
725 flow: Length-scales and orientation of the toroidal cell, *Earth and Planetary Science Letters*,
726 *479*, 284-297. http://dx.doi.org/10.1016/j.epsl.2017.09.017.

727 Lallemand, Y. Font, H. Bijwaard, and H. Kao (2001), New insights on 3-D plates interaction
728 near Taiwan from tomography and tectonic implications, *Tectonophysics*, *335*(3–4), 229-253.
729 https://doi.org/10.1016/S0040-1951(01)00071-3.

730 Lamb, S. (2011), Cenozoic tectonic evolution of the New Zealand plate-boundary zone: A
731 paleomagnetic perspective, *Tectonophysics*, *509*(3-4), 135-164.
732 https://doi.org/10.1016/j.tecto.2011.06.005.

733 Liu, L., and D. R. Stegman (2012), Origin of Columbia River flood basalt controlled by
734 propagating rupture of the Farallon slab, *Nature*, *482*(7385), 386-389.
735 https://doi.org/10.1038/nature10749.

736 Long, M. D. (2016), The Cascadia Paradox: Mantle flow and slab fragmentation in the Cascadia
737 subduction system, *Journal of Geodynamics*, *102*, 151-170.
738 https://doi.org/10.1016/j.jog.2016.09.006.

739 Long, M.D. and T. Becker (2010), Mantle dynamics and seismic anisotropy. *Earth and*
740 *Planetary Science Letters. 297.* 341-354. https://doi.org/10.1016/j.epsl.2010.06.036.

741 Lustrino, M., and M. Wilson (2007), The circum-Mediterranean anorogenic Cenozoic igneous
742 province, *Earth-Science Reviews, 81*(1-2), 1-65. https://doi.org/10.1016/j.earscirev.2006.09.002.

743 Lustrino, M., S. Duggen, and C. L. Rosenberg (2011), The Central-Western Mediterranean:
744 Anomalous igneous activity in an anomalous collisional tectonic setting, *Earth-Science Reviews*,
745 *104*(1-3), 1-40. https://doi.org/10.1016/j.earscirev.2010.08.002.

746 Ma, C., Y. Tang, and J. Ying (2019), Magmatism in Subduction Zones and Growth of
747 Continental Crust, *Diqiu Kexue - Zhongguo Dizhi Daxue Xuebao/Earth Science - Journal of*
748 *China University of Geosciences*, *44*(4), 1128-1142. https://doi.org/10.3799/dqkx.2019.026.

749 Magni, V. (2019), The effects of back-arc spreading on arc magmatism, *Earth and Planetary*
750 *Science Letters*, *519*, 141-151. https://doi.org/10.1016/j.epsl.2019.05.009.

751 Magni, V., M. B. Allen, J. van Hunen, and P. Bouilhol (2017), Continental underplating after
752 slab break-off, *Earth and Planetary Science Letters*, *474*, 59-67.
753 https://doi.org/10.1016/j.epsl.2017.06.017.

754 Melchiorre, M., J. Vergés, M. Fernàndez, M. Coltorti, M. Torne, and E. Casciello (2017),
755 Evidence for mantle heterogeneities in the westernmost Mediterranean from a statistical
756 approach to volcanic petrology, *Lithos*, *276*, 62-74. https://doi.org/10.1016/j.lithos.2016.11.018.

757 Mériaux, C. A., D. A. May, J. Mansour, Z. Chen, and O. Kaluza (2018), Benchmark of three-
758 dimensional numerical models of subduction against a laboratory experiment, *Physics of the*
759 *Earth and Planetary Interiors*, *283*, 110-121. https://doi.org/10.1016/j.pepi.2018.07.009.

760 Miller, M.S., A.A. Allam, T.W. Becker, J. F. Di Leo and J. Wookey (2013), Constraints on the
761 tectonic evolution of the westernmost Mediterranean and northwestern Africa from shear wave
762 splitting analysis, *Earth and Planetary Science Letters, Volume 375,* Pages 234-243, ISSN 0012-
763 821X, https://doi.org/10.1016/j.epsl.2013.05.036.

764 Mishin, Y. A., T. V. Gerya, J. P. Burg, and J. A. D. Connolly (2008), Dynamics of double
765 subduction: Numerical modeling, *Physics of the Earth and Planetary Interiors*, *171*(1-4), 280-
766 295. https://doi.org/10.1016/j.pepi.2008.06.012.

767 Panien, M., S. J. H. Buiter, G. Schreurs, and O. Pfiffner (2006), *Inversion of a symmetric basin:*
768 *Insights from a comparison between analogue and numerical experiments*, 253-270 pp.
769 https://doi.org/10.1144/GSL.SP. 2006.253.01.13.

770 Peral, M., Á. Király, S. Zlotnik, F. Funiciello, M. Fernàndez, C. Faccenna, and J. Vergés (2018),
771 Opposite Subduction Polarity in Adjacent Plate Segments, *Tectonics*, *37*(9), 3285-3302.
772 https://doi.org/10.1029/2017TC004896.

773 Platt, J. P., W. M. Behr, K. Johanesen, and J. R. Williams (2013), The Betic-Rif arc and its
774 orogenic hinterland: A review, in *Annual Review of Earth and Planetary Sciences*, edited, pp.
775 313-357. https://doi.org/10.1146/annurev-earth-050212-123951.

776 Pusok, A. E. and D. R. Stegman (2019), Formation and stability of same-dip double subduction
777 systems, Journal of Geophysical Research: Solid Earth, 124, 7387-7412.
778 https://doi.org/10.1029/2018JB017027.

779 Schellart, W. (2004), Kinematics of subduction and subduction-induced flow in the upper
780 mantle, *Journal of Geophysical Research B: Solid Earth*, *109*(7), B07401 07401-07419.
781 https://doi.org/10.1029/2004JB002970.

782 Schellart, W., Freeman, J., Stegman, D. et al. (2007), Evolution and diversity of subduction
783 zones controlled by slab width. *Nature 446*, 308–311. https://doi.org/10.1038/nature05615.

784 Schellart, G. S. Lister, and V. G. Toy (2006), A Late Cretaceous and Cenozoic reconstruction of
785 the Southwest Pacific region: Tectonics controlled by subduction and slab rollback processes,
786 *Earth-Science Reviews*, *76*(3-4), 191-233. https://doi.org/10.1016/j.earscirev.2006.01.002.

787 Schmeling, H., et al. (2008), A benchmark comparison of spontaneous subduction models-
788 Towards a free surface, *Physics of the Earth and Planetary Interiors*, *171*(1-4), 198-223.
789 https://doi.org/10.1016/j.pepi.2008.06.028.

790 Silver, P. (1996), Seismic anisotropy beneath the continents: Probing the Depths of Geology.
791 *Annual Review of Earth and Planetary Sciences 24:1*, 385-432.
792 https://doi.org/10.1146/annurev.earth.24.1.385.

793 Spakman, W., and M. Wortel (2004), A Tomographic View on Western Mediterranean
794 Geodynamics, *TRANSMED Atlas Mediterr. Reg. Crust Mantle*. https://doi.org/10.1007/978-3-
795 642-18919-7_2.

796 Spakman, W., M. V. Chertova, A. Van Den Berg, and D. J. J. Van Hinsbergen (2018), Puzzling
797 features of western Mediterranean tectonics explained by slab dragging, *Nature Geoscience*,
798 *11*(3), 211-216. https://doi.org/10.1038/s41561-018-0066-z.

799 Strak, V., and W. P. Schellart (2014), Evolution of 3-D subduction-induced mantle flow around
800 lateral slab edges in analogue models of free subduction analysed by stereoscopic particle image
801 velocimetry technique, *Earth and Planetary Science Letters*, *403*, 368-379.
802 https://doi.org/10.1016/j.epsl.2014.07.007.

803 Van Hinsbergen, D. J. J., R. L. M. Vissers, and W. Spakman (2014), Origin and consequences of
804 western Mediterranean subduction, rollback, and slab segmentation, *Tectonics*, *33*(4), 393-419.
805 https://doi.org/10.1002/2013TC003349.

Vergés, J., and M. Fernàndez (2012), Tethys-Atlantic interaction along the Iberia-Africa plate boundary: The Betic-Rif orogenic system, *Tectonophysics*, *579*, 144-172. https://doi.org/10.1016/j.tecto.2012.08.032.

Vignaroli, G., C. Faccenna, L. Jolivet, C. Piromallo, and F. Rossetti (2008), Subduction polarity reversal at the junction between the Western Alps and the Northern Apennines, Italy, *Tectonophysics*, *450*(1-4), 34-50. https://doi.org/10.1016/j.tecto.2008.10.019.

Wallace, L. M., S. Ellis, and P. Mann (2009), Collisional model for rapid fore-arc block rotations, arc curvature, and episodic back-arc rifting in subduction settings, *Geochemistry, Geophysics, Geosystems*, *10*(5). https://doi.org/10.1029/2008GC002220.

Wallace, L. M., C. Stevens, E. Silver, R. McCaffrey, W. Loratung, S. Hasiata, R. Stanaway, R. Curley, R. Rosa, and J. Taugaloidi (2004), GPS and seismological constraints on active tectonics and arc-continent collision in Papua New Guinea: Implications for mechanics of microplate rotations in a plate boundary zone, *Journal of Geophysical Research: Solid Earth*, *109*(5), B05404 05401-05416. https://doi.org/10.1029/2003JB002481.

Wei, W., D. Zhao, J. Xu, et al. (216), Depth variations of P-wave azimuthal anisotropy beneath Mainland China. *Sci*entific *Rep*orts *6*, 29614. https://doi.org/10.1038/srep29614

Zhang, Q., F. Guo, L. Zhao, and Y. Wu (2017), Geodynamics of divergent double subduction: 3-D numerical modeling of a Cenozoic example in the Molucca Sea region, Indonesia, *Journal of Geophysical Research: Solid Earth*, *122*(5), 3977-3998. https://doi.org/10.1002/2017JB013991.

Zhu, H., and J. Tromp (2013), Mapping tectonic deformation in the crust and upper mantle beneath Europe and the North Atlantic Ocean, *Science*, *341*(6148), 871-875. https://doi.org/10.1126/science.1241335.

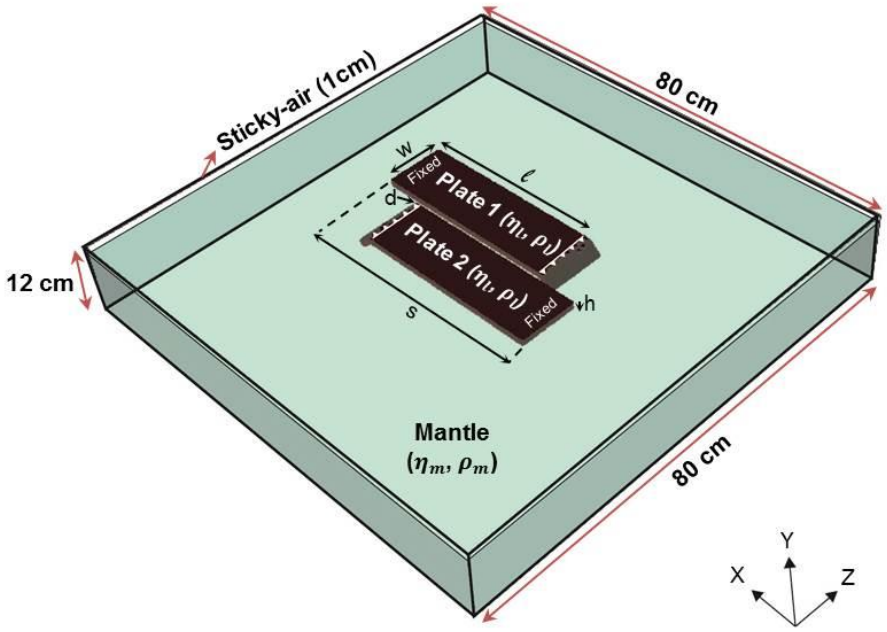

828

829 Figure 1. Model set-up: Scheme of the basic 3D numerical model of double subduction with
830 opposite polarity in adjacent segments with similar material parameters and geometry as in
831 laboratory experiments. Plates are fixed at their trailing edge to enforce rollback. Subduction is
832 initiated by a small slab reaching 3 cm depth. Different configurations varying the size of the box
833 and boundary conditions have been tested. Dimensions shown here correspond to models N2 and
834 N5 (Table 2).

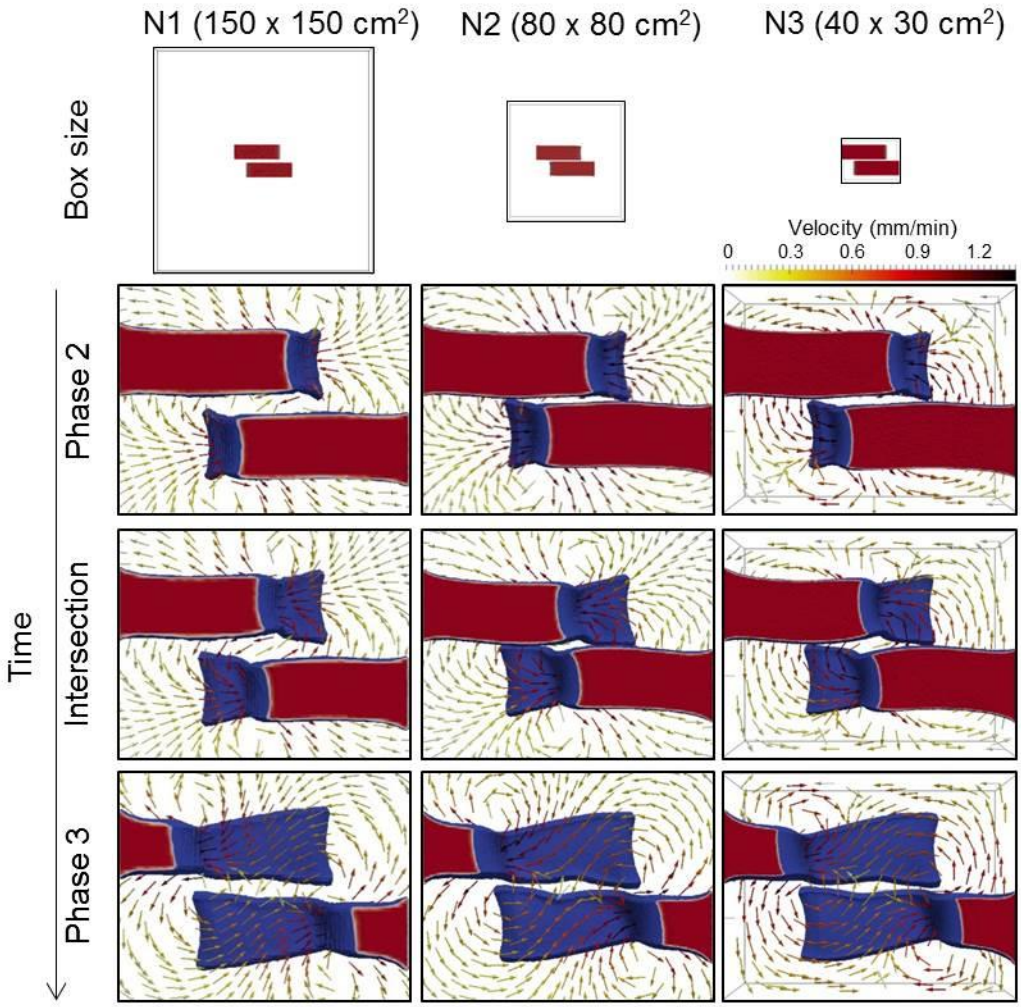

Figure 2. Influence of box-size on flow-field: Temporal evolution of numerical double subduction models with 10 cm wide plates and different box sizes (models N1, N2 and N3). Upper row displays the model box size for each column. Intersection stage corresponds to the transition between phase 2 and phase 3. Color arrows indicate the velocity field in the *x*-*z* plane (top view) at 6 cm depth from the top of the model domain. Blue and red colors denote the subducted and the buoyant parts of the plate, respectively. Note that models N1 and N2 do not show the mantle flow over the whole box.

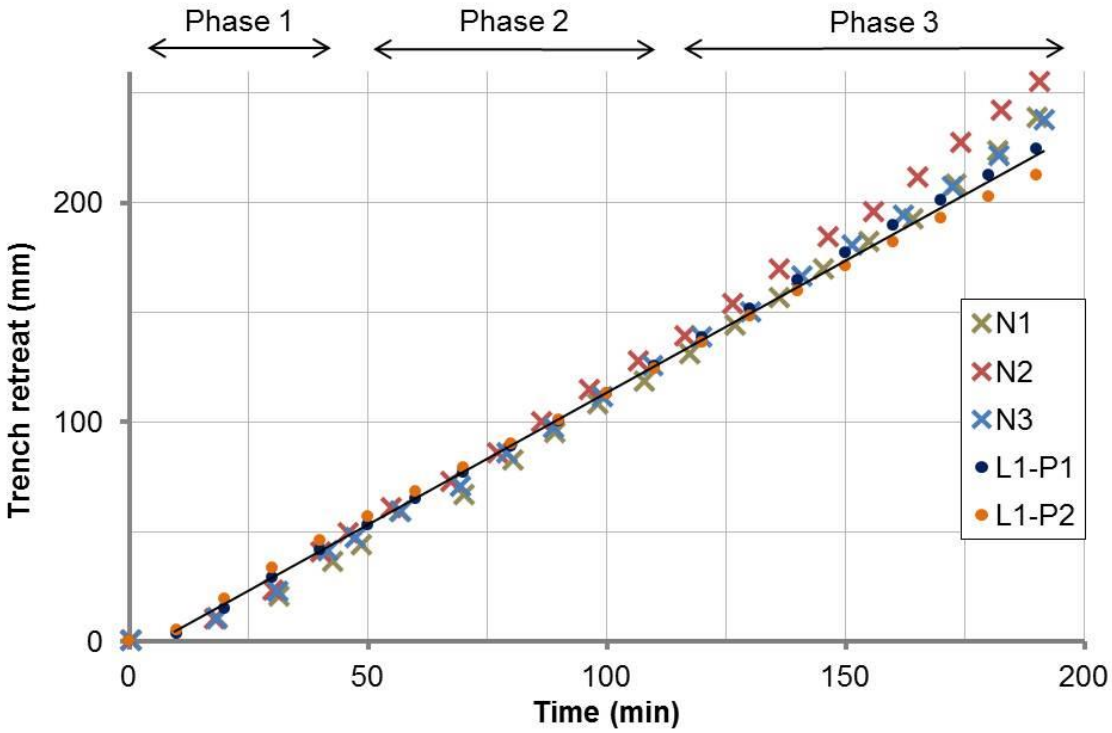

844

845 Figure 3. Influence of box-size on trench retreat: Trench retreat vs time corresponding to
846 numerical models N1 (150 x 150 cm^2), N2 (80 x 80 cm^2), N3 (30 x 40 cm^2) and laboratory
847 experiment L1 (150 x 150 cm^2). Black and orange dots: trench retreat of plates P1 and P2 of
848 analog experiment L1. Black line: linear regression for both plates of analog experiment.

849

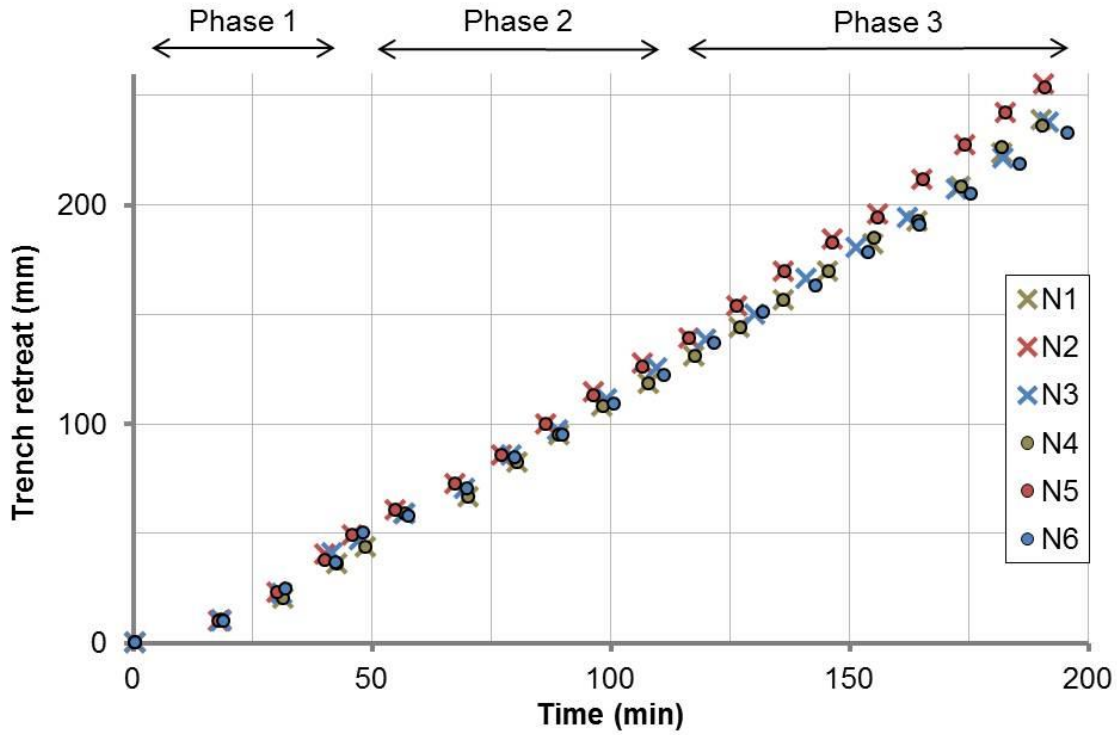

850

851 Figure 4. Influence of boundary conditions on trench retreat: Trench retreat vs time
852 corresponding to numerical models N1/N4 (150 x 150 cm^2), N2/N5 (80 x 80 cm^2) and N3/N6
853 (30 x 40 cm^2) applying different boundary conditions at the lateral walls of the box (x: free-slip;
854 o: no-slip). See Fig. 3 for laboratory results.

855

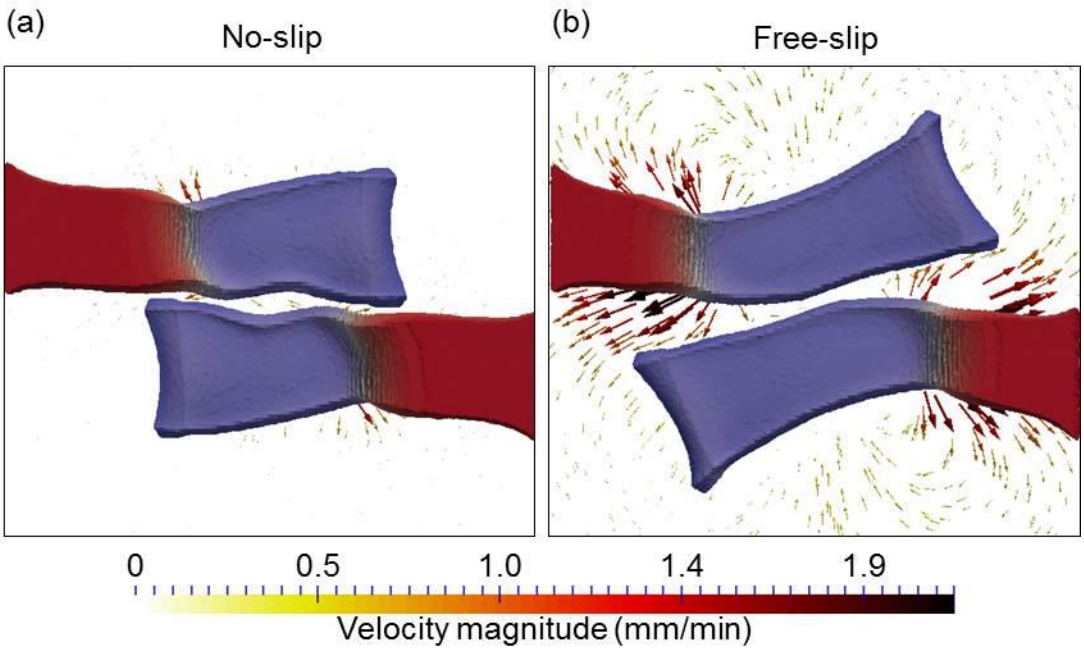

856

857 Figure 5. No-slip versus free-slip bottom boundary conditions: Numerical model of double
858 subduction with opposite polarity of 10 cm wide plates during phase 3 with no-slip (a) (model
859 N2) and free-slip (b) (model N7) boundary conditions at the bottom of the box. Color arrows
860 show the mantle flow at 11.9 cm depth from the top of the model domain.

861

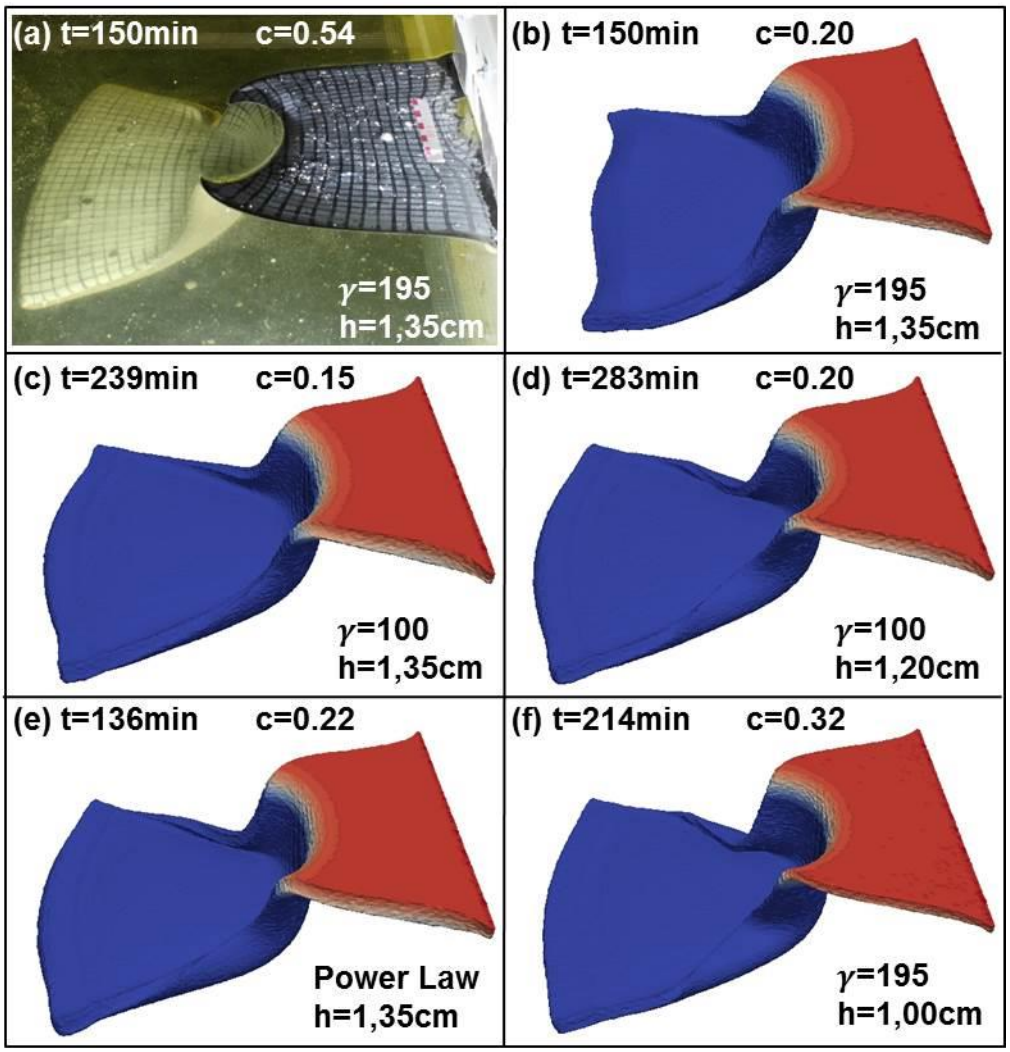

Figure 6. Rheology and plate thickness: Single subduction model of 30 cm wide plate carried out in the laboratory and by numerical modeling applying different rheology ($\gamma = \eta_l/\eta_m$) and plate thickness (h). (a) Laboratory experiment L2; (b) Numerical model N10; (c) Numerical model N12; (d) Numerical model N13; (e) Numerical model N15; (f) Numerical model N11. See parameters in Table 2. '*c*' indicates the trench curvature defined as the ratio between the chord and the sagitta of the circular segment delineated by the trench [see *Peral et al.*, 2018].

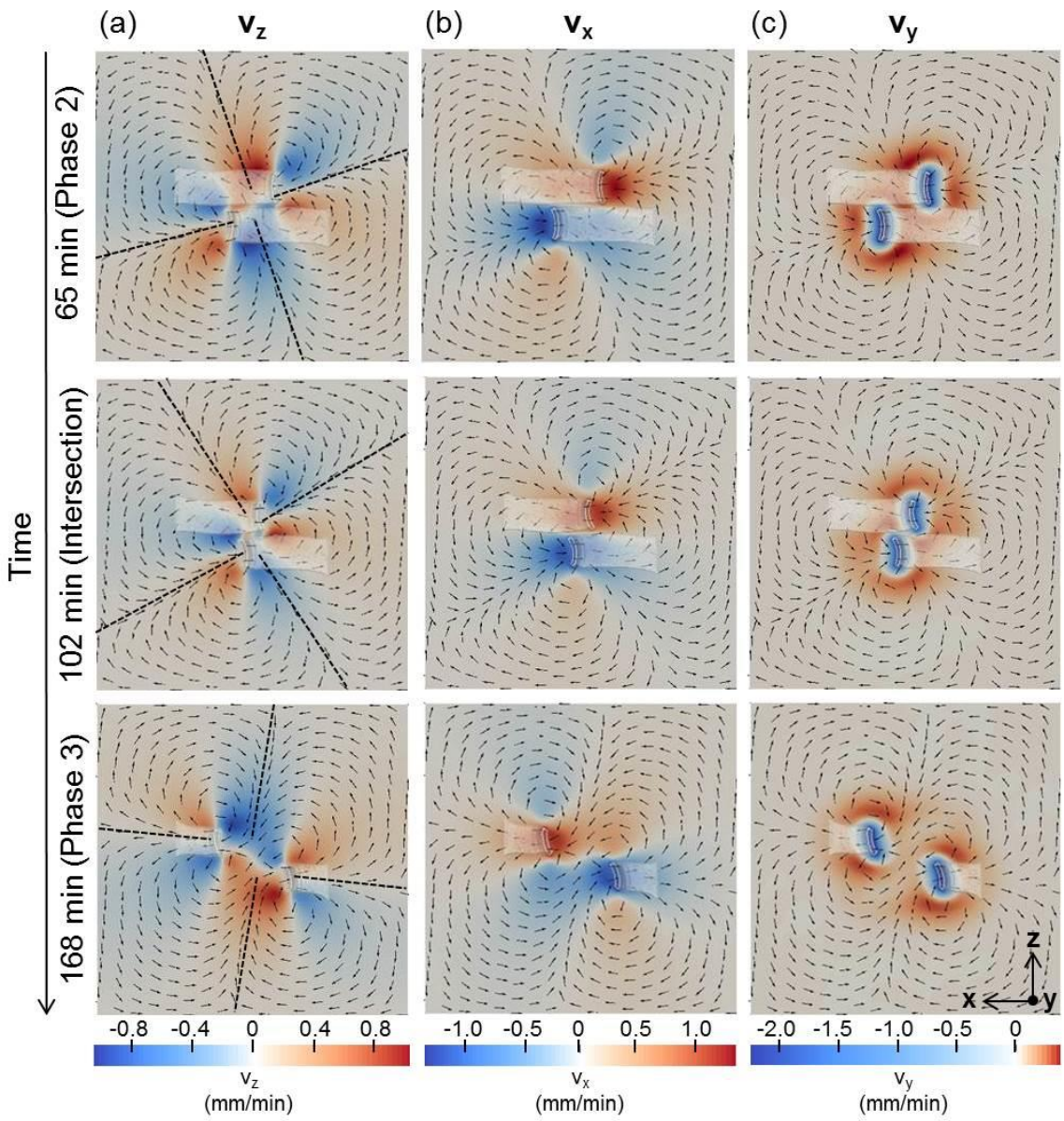

Figure 7. Temporal evolution of flow-field illustrating rotation of toroidal cells: Double subduction model N2 shown in top view. Black arrows show the flow direction in the x-z plane at 6 cm depth from the top of the model domain. Background colors indicate the velocity magnitude of the (a) v_z, (b) v_x and (c) v_y components. Stippled straight lines mark the directions of convergent and divergent flows associated with the toroidal cells, which are roughly orthogonal and rotate counterclockwise through time.

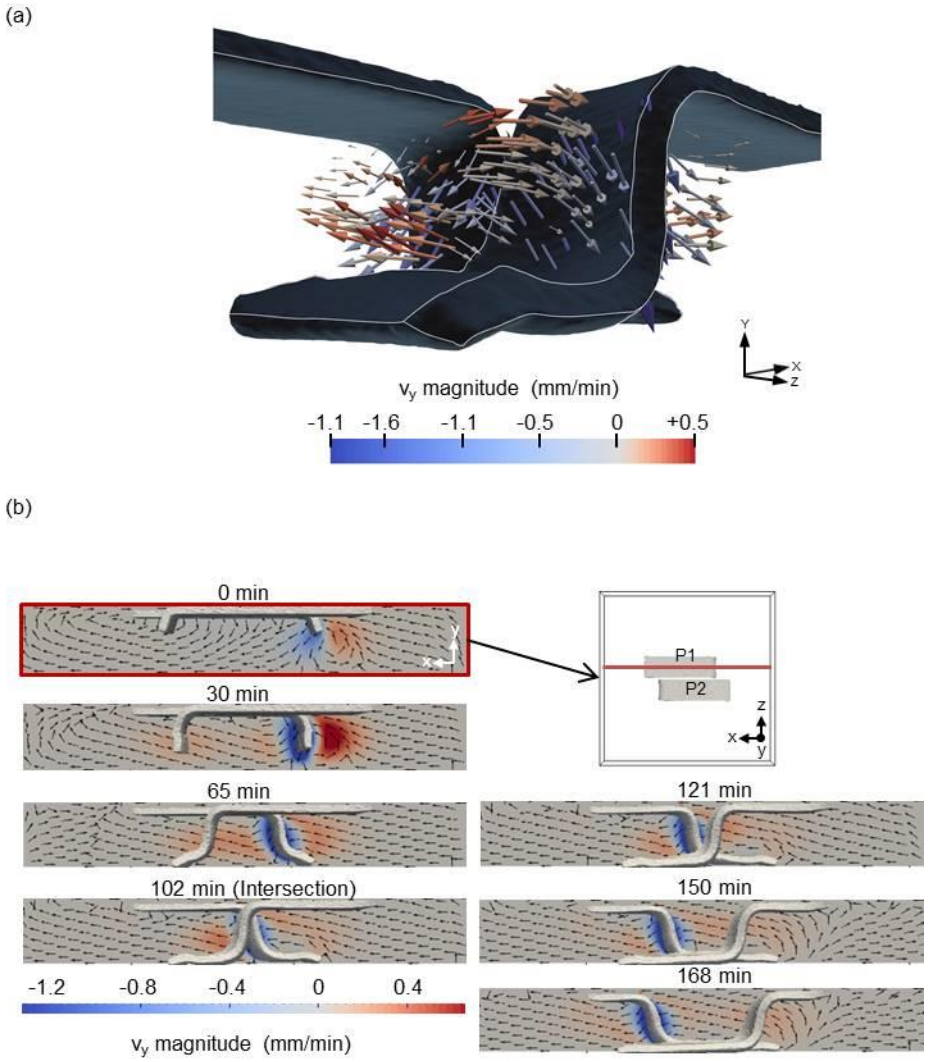

878

879 Figure 8. Velocity field in 3D of double subduction model N2: a) view of the velocity field
880 during intersection of trenches; b) time evolution of the flow direction in a cross-section (plane
881 XY) through the subducting plate 1 (see inset). Background colors indicate the vertical
882 component of the velocity field v_y where red and blue correspond to upward and downward
883 movement, respectively.

884

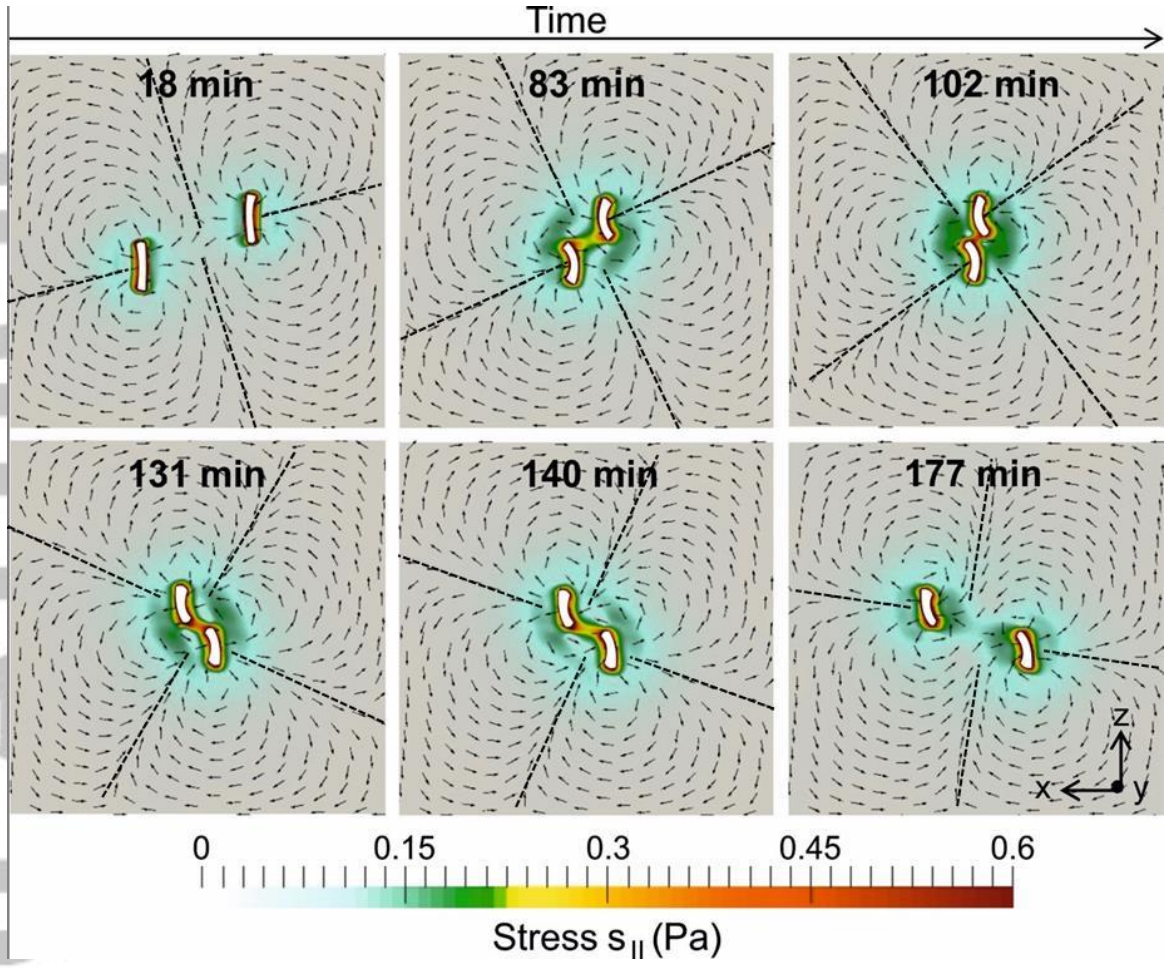

885

886 Figure 9. Effective stress: Top view of the temporal evolution of double subduction model N2.
887 Black arrows show the flow direction in the x-z plane at 6 cm depth from the top of the model
888 domain. White areas denote the location of the slabs. Background colors indicate the effective
889 stress calculated in the mantle at this depth.

890

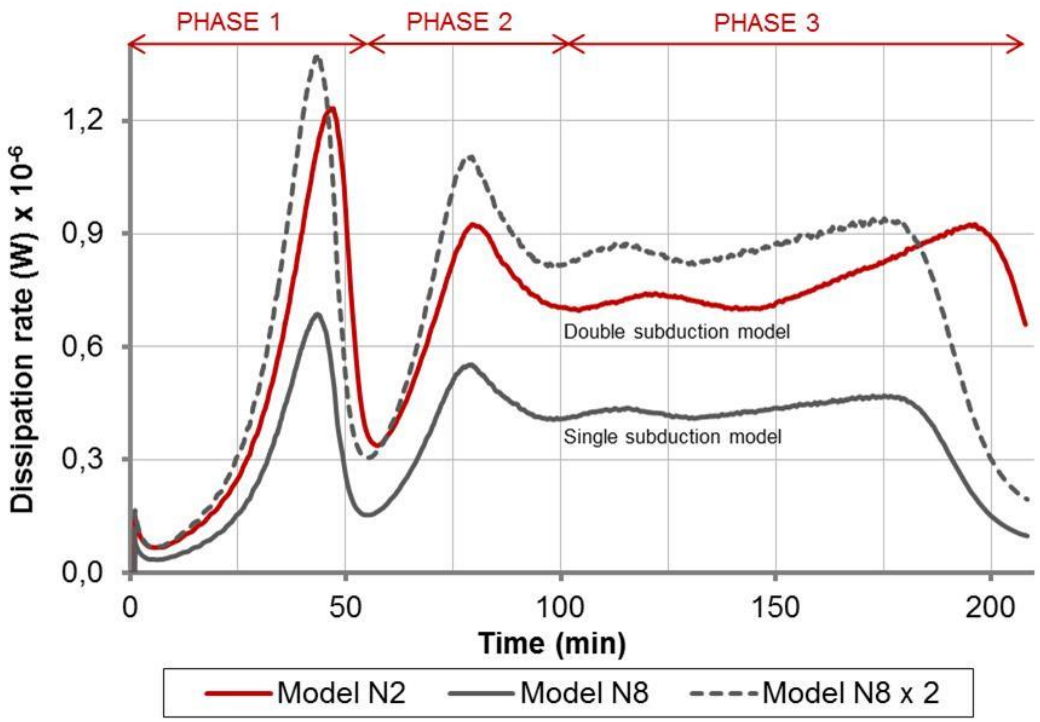

891

892 Figure 10. Energy dissipation rate associated with mantle flow of numerical models N2 (double
893 subduction) and N8 (single subduction). Dashed line would correspond to the energy dissipation
894 rate of two isolated plates. The indicated phases refer to the double subduction model.

895

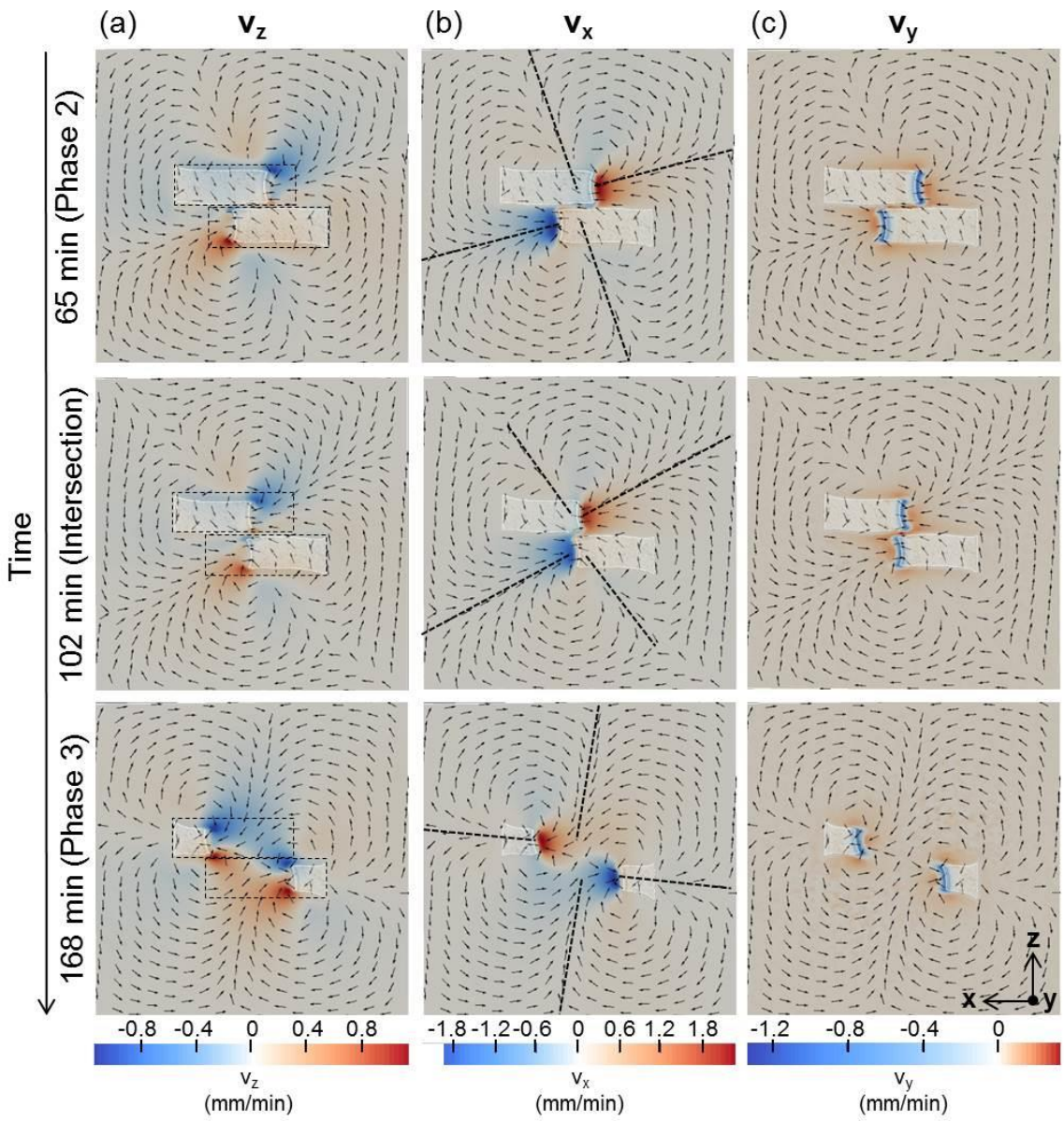

Figure 11. Plate deformation and flow in the uppermost mantle: Same as figure 7 except flow-field plotted at 1.2 cm depth. Dashed rectangles in panel (a) indicate the initial geometry of plates.

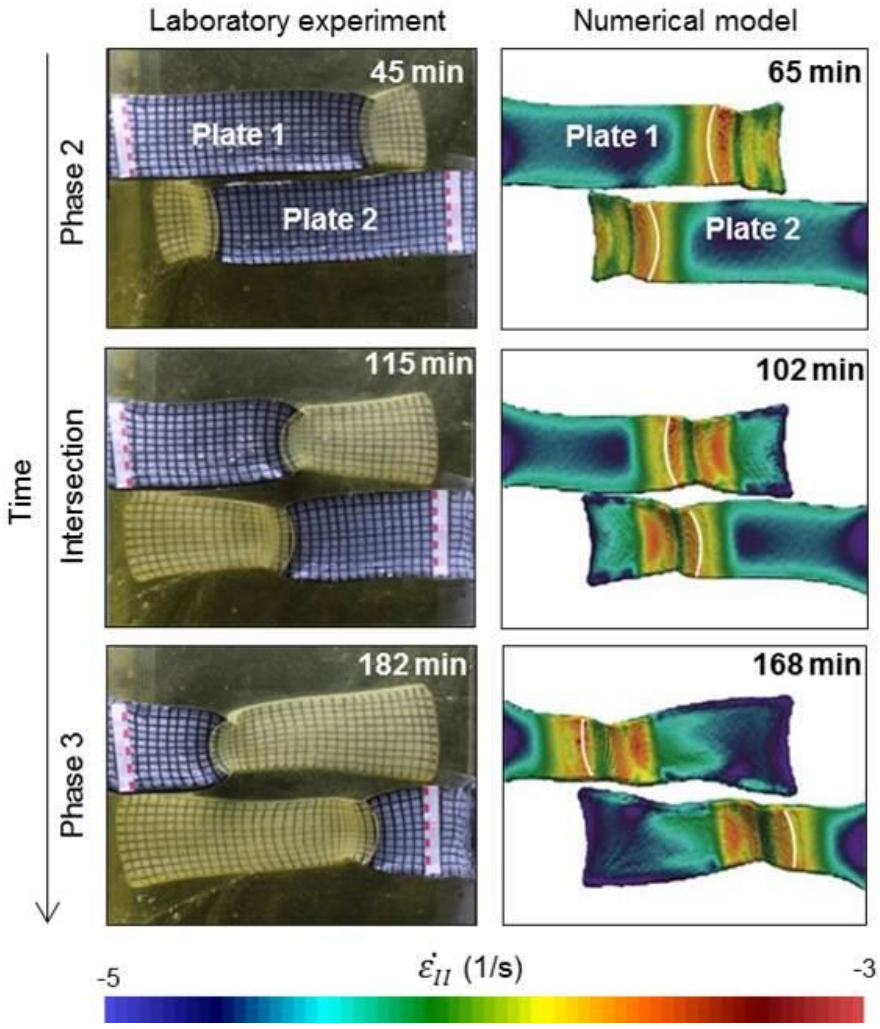

901

902 Figure 12. Strain rate: Temporal evolution of double subduction models with 10 cm wide plates
903 carried out in the laboratory (model L1) and by numerical modeling (model N2), shown in top
904 view. Colors indicate the second invariant of the strain rate (logarithm scale).

905

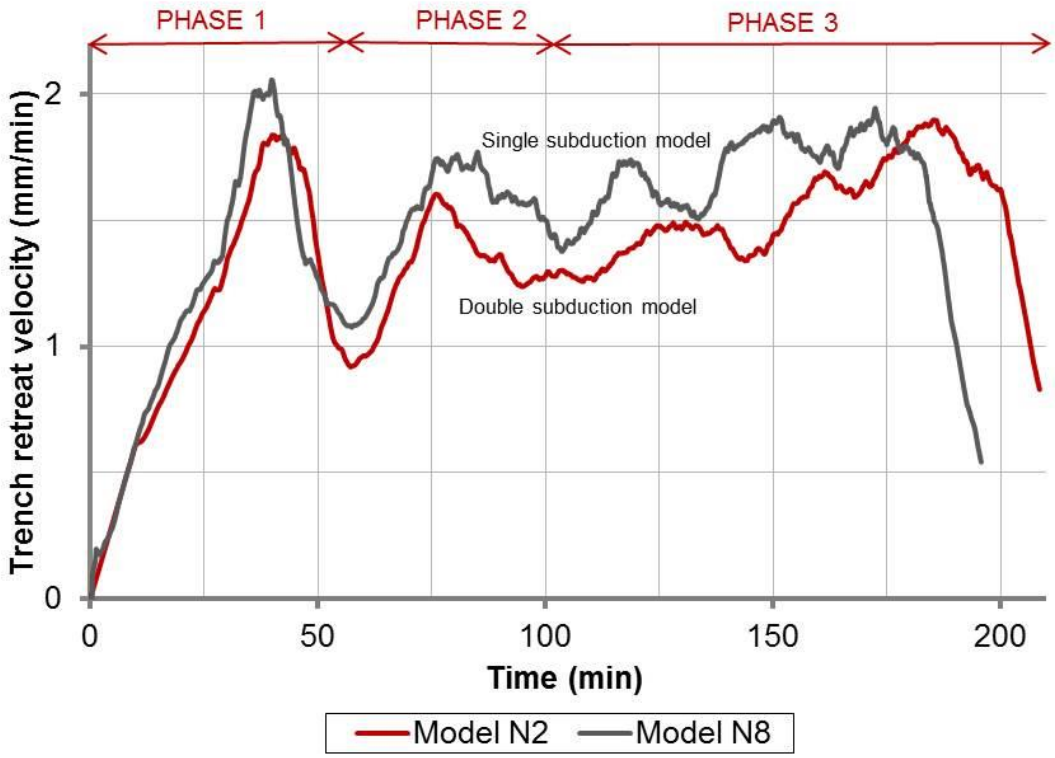

906

907 Figure 13. Trench retreat comparison between single and double subduction: Trench retreat
908 velocity vs time of numerical models N2 (double subduction) and N8 (single subduction). The
909 indicated phases refer to the double subduction model where only one plate is shown due to
910 symmetry of the initial setup.

911

Table 1. Scaling parameters in models and in Nature.

Parameter	Symbol	Units	Models	Nature
Gravitational acceleration	g	m/s^2	9.81	9.81
Upper mantle thickness	H	m	0.11	660000
Oceanic lithosphere thickness	h	m	0.01-0.0135	60000-81000
Oceanic lithosphere length	l	m	0.30	1800000
Oceanic lithosphere width	w	m	0.10-0.30	600000-1800000
Lateral distance between plates	d	m	0.01-0.02	60000-120000
Distance between trailing edges	s	m	0.39	2340000
Density contrast	$\Delta\rho=\rho_l-\rho_m$	kg/m^3	60	~75
Viscosity ratio	η_l/η_m	----	190-256	10^2-10^3
Characteristic Time: $\frac{t_{nat}}{t_{mod}} = ((\Delta\rho\, h)_{mod}\, \eta_{nat})/((\Delta\rho\, h)_{nat}\, \eta_{mod})$	t	s	60 (1 min)	1.3×10^{13} (1 My)

Table 2. Geometric characteristics and physical parameters of single and double subduction models.

NUMERICAL MODELS										
Mantle							**Plates**			
ρ_m (kg/m^3) 1445							ρ_l (kg/m^3) 1505			
Double subduction models										
Model	**d (cm)**	**l (cm)**	**W (cm)**	**h (cm)**	**Newtonian rheology** η_l (Pa·s)	**Newtonian rheology** η_m (Pa·s)	**Box domain (cm^3)**	**Resolution (cm^3)**	**Box boundary conditions** Lateral	**Box boundary conditions** Bottom
N1	2	30	10	1.35	40470	213	150x12x150	0.5x0.1x0.5	Free-slip	No-slip
N2	1	30	10	1.35	40470	213	80x12x80	0.3x0.1x0.3	Free-slip	No-slip
N3	1	30	10	1.35	40470	213	40x12x30	0.2x0.1x0.2	Free-slip	No-slip
N4	1	30	10	1.35	40470	213	150x12x150	0.5x0.1x0.5	No-slip	No-slip
N5	1	30	10	1.35	40470	213	80x12x80	0.3x0.1x0.3	No-slip	No-slip
N6	2	30	10	1.35	40470	213	40x12x30	0.2x0.1x0.2	No-slip	No-slip
N7	1	30	10	1.35	40470	213	80x12x80	0.3x0.1x0.3	Free-slip	Free-slip
Single subduction models										
Model		**l (cm)**	**W (cm)**	**h (cm)**	**Newtonian rheology** η_l (Pa·s)	**Newtonian rheology** η_m (Pa·s)	**Box domain (cm^3)**	**Resolution (cm^3)**	**Box boundary conditions** Lateral	**Box boundary conditions** Bottom
N8		30	10	1.35	40470	213	80x12x80	0.3x0.1x0.3	Free-slip	No-slip
N9		30	30	1.35	38728	151	80x12x80	0.3x0.1x0.3	Free-slip	No-slip
N10		30	30	1.35	40290	206	80x12x80	0.3x0.1x0.3	Free-slip	No-slip
N11		30	30	1.00	40290	206	80x12x80	0.3x0.1x0.3	Free-slip	No-slip
N12		30	30	1.35	38900	389	80x12x80	0.3x0.1x0.3	Free-slip	No-slip
N13		30	30	1.20	38900	389	80x12x80	0.3x0.1x0.3	Free-slip	No-slip
N14		30	30	1.00	38900	389	80x12x80	0.3x0.1x0.3	Free-slip	No-slip
Model		**l (cm)**	**w(cm)**	**h (cm)**	**Power-law rheology** η_0 (Pa·s)	**n**	**Power-law rheology** η_m (Pa·s)	**Box domain (cm^3)**	**Resolution (cm^3)**	**Box boundary conditions** Lateral / Bottom
N15		30	30	1.35	1000	1.5	206	80x12x80	0.3x0.1x0.3	Free-slip / No-slip
LABORATORY EXPERIMENTS										
Double subduction model										
Model	**d (cm)**	**l (cm)**	**W (cm)**	**h (cm)**	**Newtonian rheology** η_l (Pa·s)	**Newtonian rheology** η_m (Pa·s)	**ρ_l (kg/m^3)**	**ρ_m (kg/m^3)**	**Box domain (cm)**	
L1	0.5	30	10	1.35	40470	213	1499	1445	150x11x150	
Single subduction model										
Model		**l (cm)**	**W (cm)**	**h (cm)**	**Newtonian rheology** η_l (Pa·s)	**Newtonian rheology** η_m (Pa·s)	**ρ_l (kg/m^3)**	**ρ_m (kg/m^3)**	**Box domain (cm)**	
L2		30	30	1.35	40290	206	1511	1445	150x11x150	